Title: Nickel in olivine as an exploration indicator for magmatic Ni-Cu sulfide deposits: a data review and re-evaluation.
Manuscript Number: 8327R1
Authors: Stephen Barnes, CSIRO Yajing Mao, Institute of Geology and Geophysics, Chinese Academy of Sciences Ana Jesus, Universidade de Lisboa Sheng-Hong Yang, University of Oulu Valentina Taranovic, CSIRO Wolfgang Maier, Zhuo-Sen Yao, Dept Earth Sciences

Nickel in olivine as an exploration indicator for magmatic Ni-Cu sulfide deposits: a data review and re-evaluation

REVISION 1

Stephen J. Barnes[1], Zhuo-Sen Yao[2], Ya-Jing Mao[3], Ana P. Jesus[4], Shenghong Yang[5], Valentina Taranovic[1,7], Wolfgang D. Maier[6].

[1]CSIRO Mineral Resources, 26 Dick Perry Ave., Kensington, WA 6151 Australia. Steve.barnes@csiro.au [2]Department of Earth Sciences, Carleton University, Ottawa, Canada. yaozhuosen@gmail.com [2]Key Laboratory of Mineral Resources, Institute of Geology and Geophysics, Chinese Academy of Sciences (CAS), Beijing 100029, China. maoyajing@mail.iggcas.ac.cn. [4]Faculdade de Ciências, Universidade de Lisboa, Lisbon, Portugal. apjesus@fc.ul.pt [5]Oulu Mining School, Univ. of Oulu, Finland. shenghong.yang@oulu.fi. [6]Dept. of Earth Sciences, Univ. of Cardiff, Wales. maierw@cardiff.ac.uk. [7]tinatskg@gmail.com.

Abstract

Nickel contents of olivine have been widely used as petrogenetic indicators and as fertility indicators for magmatic sulfide potential of mafic-ultramafic intrusions, on the assumption that olivines crystallized from magmas that had equilibrated with sulfide liquid should be relatively depleted in Ni compared with a sulfide-free baseline. This has given rise to a large accumulation of data that is brought together here, along with data on volcanic olivines, to critically evaluate the effectiveness of the approach. We identify multiple sources of variance in Ni content of olivine at given Fo content, including: variability in mantle melt composition due to depth, water content (and possibly source); subsequent fractional crystallization with and without sulfide; recharge and magma mixing; batch equilibration between olivine and sulfide at variable silicate-sulfide ratio (R) and olivine/liquid ratio; and subsequent equilibration during trapped liquid crystallization in orthocumulates. Baselines for Ni in olivine in relation to Fo content are somewhat lower in orogenic belt settings relative to intrusions in continental Large Igneous Provinces (LIPs). This is probably related to differences in initial parent magma compositions, with plume magmas generally forming deeper and at higher temperatures. No clear, universal discrimination is evident in Ni in olivine between ore-bearing, weakly mineralized and barren intrusions even when tectonic setting is taken into account. However, sulfide-related signals can be identified at intrusion scale in many cases. Low-R factor, low-tenor sulfides are associated with low-Ni olivines in a number of examples and these cases stand out clearly.

Anomalously high-Ni olivines are a feature of some mineralized intrusions, in part due to trapped liquid reaction effects. However, in some cases, this mechanism cannot account for the magnitude of enrichment. In these cases, enrichment may be due to re-entrainment of “primitive” Ni-rich sulfide by a more evolved Fe-rich magma, driving the olivine to become Ni-enriched due to Fe-Ni exchange reaction between sulfide and olivine during transport. An extreme case of this process may account for ultra-Ni enriched olivine at Kevitsa (Finland), but more subtle signals elsewhere could be positive indicators. A lack of clear mineralized/barren distinction in specific groups of related intrusions, e.g. the deposits of NW China or the Kotalahti Belt in Finland, may well be due to “false negatives” where undiscovered mineralization exists in specific intrusions or in their feeder systems, or may also be due to a multiplicity of confounding factors. Wide variability of both Fo and Ni between related intrusions at regional scale may be a useful regional prospectivity indicator, more than an intrusion-scale discriminant, and is certainly informative as a petrogenetic indicator. In general, the use of Ni-olivine as a fertility tool is more likely to generate false negatives than false positives, but both are possible, and the technique should be used as part of a broader weight-of-evidence approach.

Keywords: magmatic sulfides, nickel deposits, mantle melting.

Introduction

The Ni content of olivine has been used over several decades as an indicator of potential host rocks to magmatic Ni-Cu sulfide deposits (Häkli, 1971; Naldrett et al., 1984; Li and Naldrett, 1999; Barnes et al., 2004; Makkonen et al., 2008; Barnes and Fiorentini, 2012; Le Vaillant et al., 2016). More generally, Ni in olivine has been widely used as a petrogenetic indicator to infer mantle magma sources (Sobolev et al., 2005; Sobolev et al., 2007; Li and Ripley, 2010) and deep-seated petrogenetic processes (Hart and Davis, 1978; Zhang et al., 2005; Herzberg et al., 2016; Matzen et al., 2017b; Gleeson and Gibson, 2019). Its potential usefulness as a prospectivity indicator arises from the compatible and chalcophile character of Ni, which has a strong tendency to partition both into olivine and much more strongly into sulfide liquid from coexisting silicate melt (Duke, 1979; Naldrett et al., 1984; Kiseeva and Wood, 2015; Yao et al., 2018). Consequently, competition for Ni between co-precipitating sulfide and olivine should produce olivine depleted in Ni relative to olivines that have never “seen” sulfide liquid. This effect was modelled in detail in the only previous global review of the topic (Li et al., 2007). However, more recent experimental data on the strong dependency of partitioning behaviour of Ni into olivine with temperature (Li and Ripley, 2010; Matzen et al., 2017a; Matzen et al., 2017b; Pu et al., 2021) together with effects of recharge and magma mixing (Gleeson and Gibson, 2019) introduce important confounding factors into the interpretation. Furthermore,

olivine compositions may be modified considerably by post-cumulus processes (Barnes, 1986) which can generate Ni enrichment in some circumstances (Barnes and Naldrett, 1985; Li and Naldrett, 1999; Ding et al., 2010). These multiple factors, among others considered here, have not been fully considered in previous studies,

In this contribution, we combine an empirical data-driven approach with quantitative modelling of the various factors controlling olivine compositions in sulfide-saturated and undersaturated magmas. We employ a large compilation of data on Ni in olivine from volcanic and intrusive rocks, including all the published data we have been able to locate on mineralized and unmineralized mafic-ultramafic intrusive rocks over a wide range of ages and tectonic settings. From this dataset, we assess whether systematic differences exist that would enable reliable discrimination of mineralized intrusions. Such a tool would potentially be applicable in target selection at the early stage of regional exploration campaigns and also in vectoring towards mineralization in well-explored terranes. This approach has already been investigated for komatiite-hosted magmatic sulfide systems and shown to be effective at prospect scale in some cases, such as the Agnew-Wiluna Belt of the Yilgarn Craton (Barnes and Fiorentini, 2012; Le Vaillant et al., 2016), although signals are commonly confounded by flushing of mineralized lava channels post ore formation (Barnes et al., 2013b). Here we focus primarily on application to mineralization within small mafic-ultramafic intrusions in continental large igneous provinces (LIPs) and orogenic belts.

Method

Olivine chemistry data has been compiled from large number of literature sources listed in Supplemental Table 1 and from the GEOROC online database (http://georoc.mpch-mainz.gwdg.de/georoc/)(Lehnert et al., 2000; Sarbas, 2008). Data plotting and data density contouring was done with the ioGas geochemical plotting software. In all cases data are from electron microprobe microanalysis, which typically reports Ni contents down to hundreds of ppm with precisions around 5-10% of measured abundance. Tabulation of individual precision estimates for the many dozens of different data sources was not attempted, but readers are referred to original sources (Supplementary Table 1) for further details. A full listing of data compilation used in this study is available at https://zenodo.org/record/5787901 or via the CSIRO Data Access Portal at doi: (*to be advised*).

Samples were classified on the basis of volcanic/intrusive status (volcanic, small intrusions and large layered intrusions); combined tectonic setting and age (large igneous provinces and convergent margins, Phanerozoic and Proterozoic) and for intrusion samples, three categories of mineralization status of the host intrusion: M(ineralized), containing economic accumulations of Ni-Cu sulfide;

(D)isseminated, containing economic or sub-economic disseminated Ni-Cu sulfide mineralization only; and (B)arren, either no sulfide mineralization at all as far as is known, or only minor disseminations. These distinctions are inevitably somewhat arbitrary and based on best available data. In many of the plots, summary "data clouds" for particular groupings are represented as smoothed kernel data density contours determined in the IoGas plotting software. In most cases except where stated contours enclose the 50^{th} and 90^{th} percentiles on data point density.

Modelling calculations follow the procedures and assumptions of Yao et al. (2018). These are described in appendix 1.

Results

Background olivine compositions in Phanerozoic basalts

Compositions of olivine phenocrysts in basalts provide a useful baseline for comparison, in that they are least likely to have been modified by the processes that affect cumulate rocks in intrusions. A dataset of over 20,000 analyses, assembled by Sobolev and co-workers (Sobolev et al., 2007), is shown in summary form in Figure 1 along with additional data from convergent margin basalts from the GEOROC database (Sarbas, 2008). Wide variability was noted by Sobolev et al. (2007) in relation to tectonic setting, such as basalts from continental large igneous provinces (CLIPS) and from intra-oceanic plumes associated with old, thick oceanic lithosphere. This gives rise to distinctly different baseline ranges for CLIPS, oceanic LIPs and hotspot chains (OLIP) and MORBs, which are distinctly lower in olivine Ni than the other two categories for given Fo content. Since many of the potential target intrusions for magmatic sulfide deposits occur within mid-plate LIPs, the CLIP basalt dataset (Figure 1B) makes a useful baseline for comparison for these cases. The approximate 75^{th} percentile data density contour on the CLIP data (black outline on Figure 1 B,C) (with the outlying Gudchichinsky Picrite suite from Siberia excluded) is reproduced in some of the diagrams that follow.

Figure 1

Volcanic olivine compositions from convergent margins (Figure 1D) show a somewhat contrasting pattern with the LIP data cloud. The bulk of the data sets overlaps with the LIP data, but clusters of points fall both well above and well below. Oceanic arc olivines have a distinctly bimodal distribution, whereby a distinct group of primarily oceanic arc-associated olivines falls well below the LIP cloud at the higher Fo end (Fig. 1D).

Comparison of intrusion hosted olivines between tectonic settings

Modelling of olivine compositions from variably hydrated and variable depth sources (see below) indicates that we would expect significantly different baseline trends for magmas from deep-

sourced continental LIPs relative to magmas formed by shallow flux melting in arcs. The effect of melting depth (melting beneath thick and thin lithosphere) was pointed out by (Sobolev et al., 2005, 2007). For this reason we combine continental LIP and intracratonic layered intrusions such as Bushveld together as one category, and orogenic belts with likely arc associations as another (Figure 2) in establishing baselines for comparison of mineralized versus unmineralized intrusions. A caveat is needed here in that in some cases "orogenic belt" localities may be sampling plume magmas emplaced along craton margins and caught up in collisional events; this is particularly an issue in highly deformed Proterozoic orogens such as the Albany-Fraser Orogen in Western Australia. For purposes of this study, we include all such occurrence in the Orogenic Belt category but acknowledge the strong possibility of misclassification. Data for unmineralized intrusions only are plotted in Figure 2. Layered intrusions containing stratiform PGE Reef mineralization are considered unmineralized for this purpose, on the grounds that the magmas parental to the reefs could not have interacted previously with large proportions of sulfide liquid.

A major problem in empirical comparisons of this type is a sampling bias towards mineralized intrusions; they tend to be more common subjects of academic study than barren intrusions and exploration companies drill more holes into sulfide-bearing bodies. Furthermore, there may well be a false negative bias in that where an intrusion is known to contain sulfides its classification is clear, whereas "barren" intrusions may simply contain as yet undiscovered mineralization. As an additional baseline for comparison, we have therefore included a field for expected olivine compositions derived by fractional crystallization from the plausible range of mantle-derived basaltic magmas generated by 10% or more partial melting, based on the modelling of Yao et al. (2018). This field is labelled "MSFM" for "model sulfide free mantle melts" in Figure 2 and subsequent Ni vs Fo plots. The derivation of these model values is discussed in detail below.

Figure 2.

The data clouds shown in Figure 2 are clearly distinct between the continental LIP (CLIP+LMI) and Orogenic Belt (OB) categories, with the latter having consistently lower Ni for the same Fo content. We therefore need to consider different baselines for these two different tectonic settings. Furthermore, the data set for CLIP-associated intrusions shows a considerably broader spread than the field for volcanic olivines, particularly at low Fo contents.

In the following sections, we compare olivine compositions for mineralized and unmineralized intrusions from CLIP and OB settings. Implicit in this comparison is the major uncertainty of "false negatives" as noted above, which should be borne in mind through the discussion.

Mineralized vs barren, CLIP settings

Figure 3 shows a comparison of data points for olivines in variably mineralized mafic-ultramafic intrusions in intraplate continental Large Igneous Province (CLIP) settings (including large intracratonic layered intrusions), plotted over the data density cloud for unmineralized CLIP-associated intrusions. In this plot and those that follow, intrusions hosting economic sulfide-rich mineralization are plotted as red symbols, with symbol shapes indicating locality, while green symbols denote intrusions containing disseminated and/or minor subeconomic mineralization only. The bulk of the data fall within the "unmineralized" data cloud, with three localities as major exceptions. Kabanga (Tanzania) shows consistently strong Ni depletion in the main ore-hosting intrusion (Maier et al., 2010; Maier et al., 2011). Voisey's Bay (Labrador, Canada, red circles) defines a field of widely varying Ni and Fo with Fe-rich olivine compositions extending to below Fo45. Nickel contents vary by a factor of up to 7 over the same Fo. In the Kevitsa Intrusion (northern Finland) the range of variability is a factor of 20 over a limited range in Fo. As well as a cluster of strongly depleted olivines, the Kevitsa dataset includes some extreme examples of Ni enrichment (Yang et al., 2013) falling outside the scale limits of this plot; these are discussed further below in the case-study section below. The main conclusion at this stage is that there is no universal evidence for consistent Ni depletion in mineralized compared with unmineralized intrusions, but distinct signals can be recognized in some specific cases. Wide variability for limited range in Fo appears to be the most consistent signal in mineralized intrusions. It is noteworthy that a large portion of the data cloud falls above the theoretical field (MSFM field on Figure 3) for olivines derived from sulfide-free mantle melts.

Figure 3.

Mineralized vs barren, orogenic belt settings

An exactly equivalent comparison to that in Figure 3 is shown in Figure 4 for combined Phanerozoic and Proterozoic orogenic settings (bearing in mind that some of the localities included in this category could be misallocated plume associations). The same conclusion applies: there is no clear evidence for consistent Ni depletion in mineralized compared with unmineralized intrusions. However, as in the CLIP category, mineralized intrusions occupy a wider range, with Ni falling both above and below the unmineralized baseline and show a wide variability of Ni for similar Fo contents. The most clearly anomalous mineralized intrusions are the Savannah intrusions in the Halls Creek orogen that show localized strong enrichment, and a group of intrusions (Moxie, Maine; St Stephen, New Brunswick and Rana, Northern Norway) within the Appalachian-Caledonide orogen that shows consistently Ni depleted olivine (Figure 4B). The Beja intrusion, Portugal, host to minor

disseminated sulfides (Jesus et al., 2020), straddles the 90th percentile “barren” contour but contains a high proportion of significantly Ni-depleted olivines at low Fo. We consider some of these localities further below as case studies. The Xiarihamu deposit in the East Kunlun orogenic belt in Tibet shows a distinctive signal of widely variable Ni at a restricted range of high Fo contents, somewhat similar to the Poyi intrusion in the Central Asia Orogenic Belt in China. Comparing Phanerozoic and Proterozoic settings, Phanerozoic intrusions appear to be more likely to show recognisable Ni depletion, as noted by Jesus et al. (2020). This may be an association with depth of emplacement, noting that several of the Proterozoic intrusions (Savannah, Kotalahti Belt, Nova) were emplaced at mid to lower crustal depths.

Compared with the theoretical model field for olivines derived from sulfide-free basalts (MSFM outline), evidence for Ni depletion is seen in the localities mentioned above, along with some samples from Xiarihamu, Ntaka Hill, Nova and several of the Chinese CAOB deposits. Samples from Savannah plot well above the MSFM field.

Figure 4.

Comparison within individual magmatic provinces

In this section, we consider some specific examples from both orogenic and CLIP categories where multiple intrusions co-exist within a restricted province with and without significant mineralization.

LIP related: Kabanga–Musongati–Kapalagulu Belt, Tanzania

The Kabanga deposit is located in a relatively small chonolith-style intrusion within the 1.4 Ga Kabanga–Musongati–Kapalagulu (KMK) mafic–ultramafic belt that extends for >500 km from Uganda to Lake Tanganyika in the Great Lakes region of East Africa (Deblond and Tack, 1999; Evans et al., 2000; Duchesne et al., 2004; Maier et al., 2007; Maier et al., 2010). This belt is considered to form part of a LIP developed along the NW margin of the Tanzanian Craton (Mäkitie et al., 2014). The belt contains both relatively large, mafic-ultramafic layered intrusions of several km thickness and tens of square km in surface and subsurface outcrop (e.g., Musongati and Kapalagulu) and numerous sills and chonolith bodies consisting largely of harzburgite, pyroxenite and gabbronorite, with thicknesses on the order of m to hundreds of m (e.g., Kabanga).

The Kabanga North-MNB body, one of the smallest intrusions in the belt, has a tubular chonolith morphology measuring up to 150 m in diameter. The body has been delineated by drilling for ~1.4 km in a NE–SW direction. The Kabanga Main intrusion is a sill-like body with a relatively narrow (2km), trough-like lower portion and an upper segment of greater width (~4km). Its thickness may be on the order of 500m. The ~500-m-thick MNB body was discovered in 2001 while drilling for extensions of the Kabanga North body. The MNB extends over >2 km strike length and bears

considerable similarity to the Kabanga Main body. It may thus represent the extension of Kabanga Main at depth. The Block 1 intrusion, 4 to 5 km to the SW of Kabanga Main, consists of a thick (~ 800m) pile of mafic-ultramafic cumulates containing abundant disseminated low-tenor sulfides.

The heavily mineralized intrusions of the Kabanga locality stand out clearly as having strongly Ni depleted olivines, with the most advanced depletion being in the Upper KM Sill, Block 1 and the MNB body (Figure 5). This is the clearest example in the entire dataset of strong Ni depletion associated with high degrees of crustal contamination and abundant sulfides having low Ni tenors. Kabanga sulfides have low Ni (<1–3 wt%), Cu (~0.1–0.4 wt%), and PGE contents (≪1 ppm), high Ni/Cu (5–15), and low Ni/Co (10–15) and Pd/Ir (2–20). Sulfides with higher metal contents (up to ~5% Ni, 0.8% Cu, 10 ppm PGE) are found in only one unit from Kabanga North, which significantly has markedly less Ni depleted olivine, albeit still depleted relative to the CLIP "Barren" baseline. The observed metal contents of the Kabanga sulfides are consistent with segregation of magmatic sulfides from fertile to strongly metal-depleted magmas, at intermediate to very low mass ratios of silicate to sulfide liquid (R factors) of approximately 10–400.

The Kapalugulu intrusion, approximately 300 km south of Kabanga, is a large layered intrusion containing chromitite and associated PGE concentrations. It contains sulfide mineralization only in a proposed feeder zone and shows undepleted olivines in samples from the unmineralized layered cumulate sequence.

Figure 5.

Proterozoic Orogenic Belt: Halls Creek Orogen, Australia. The Savannah (formerly Sally Malay) and Savannah North deposits, along with the smaller Copernicus deposit, are located within a belt of 1.8 Ga mafic and mafic-ultramafic intrusions, the Sally Malay Suite, within the Halls Creek Orogen of Western Australia (Mole et al., 2018; Le Vaillant et al., 2020). The magmatism is thought to be related to a slab break-off event during the collision of the North Australian and Kimberley Craton (Kohanpour et al., 2017). The Savannah deposit occupies the lower edge of a now rotated bladed dyke (Barnes and Mungall, 2018) and the adjacent Savannah North deposit occupies a basal contact position within a separate small layered intrusion with probable funnel geometry. A group of petrographically similar intrusions within about 10 km of Savannah has been sampled by regional scale exploratory drilling, which has located only minor occurrences of disseminated sulfide. On this basis, Savannah and Savannah North samples represent the mineralized category while the remainder are considered barren.

Most of the olivines analysed from this suite fall within the “barren” baseline for orogenic settings (Figure 6), and Savannah North is indistinguishable in olivine chemistry from the barren Dave Hill and Wilson’s Creek bodies, aside from one data cluster at high Fo and low Ni that probably does reflect sulfide-related depletion. The notable exception is the Savannah Intrusion, which contains substantially more Ni enriched olivines within the layered peridotite and olivine norite layers that occupy the interior of the dyke. These rocks are primarily mesocumulates, and no systematic difference in olivine composition is recognisable with sulfide or olivine mode, such that the displacement from the cluster of Savannah North olivines cannot simply be explained by trapped liquid equilibration. The Savannah Intrusion evidently formed from a more Ni rich carrier magma than the other components of the Sally Malay suite. However, this contrast is not evident in the Ni tenors of the Savannah and Savannah North sulfide rich ores, which are 3.5-5 wt% and 2-3.5 wt% respectively. Both orebodies are strongly PGE depleted (Le Vaillant et al., 2020) implying prior extraction of sulfide liquid.

For this data set, we have also investigated the extent to which Fo-Ni variability is distinguishable on the basis of the sulfide content of individual samples (Figure 6B). Most of the analysed samples from the Savannah intrusion are sulfide-free, from the interior of the intrusion, showing the distinctive Ni enrichment characteristic of this body, but some mineralized samples are also Ni enriched. There is an almost complete overlap (with the exception of the highest Fo sample) between sulfide-bearing and sulfide-free samples in the Savannah North intrusion. This confirms that recognition of indicative Fo-Ni signals does not rely on sampling sulfide-bearing rocks.

Figure 6.

Phanerozoic Orogenic Belt, Central Asian Orogenic Belt, NW China. About a dozen economic magmatic Ni-Cu sulphide deposits occur at the southern margin of the Central Asian orogenic belt (CAOB) in NW China (Mao et al., 2008; Lu et al., 2019), with a few deposits occur in the southeasternmost part of CAOB, such as the Hongqiling deposit in NE China (Wei et al., 2013; Lu et al., 2019). These NW China deposits could be classified into four groups by spatial distribution: the Beishan, Central Tianshan, Eastern Tianshan, and south Chinese Altai groups from south to north. over a total distance of close to 1000 kilometres. They were predominately formed in the Permian (Qin et al., 2011; Su et al., 2011). The host rocks of these NW China deposits are enriched in hydrous phases and show arc-like geochemical characteristics, suggesting that the related magmas were derived from metasomatized mantle sources which have been modified by the subduction events prior to the Permian. Most researchers propose that the Permian magmatism in the south (Beishan, Central Tianshan, and Eastern Tianshan) of NW China was associated with the partial melting of metasomatized mantle driven by either the coeval Tarim mantle plume (Qin et al., 2011; Su et al.,

2011) or asthenosphere upwelling induced by lithosphere delamination (Song et al., 2011a; Zhang et al., 2011). The Permian magmatism in the Chinese Altai is thought to be triggered by a slab break-off event (Zhang et al., 2009; Li et al., 2012). Ore-hosting magmatic bodies of these deposits come in a variety of shapes, i.e. elongated rhomboid, kernel-shaped flares, tube-like or dyke-like, and have surface areas less than 2 km^2. Several have been interpreted as variants on the theme of "blade-shaped dykes" (Barnes and Mungall, 2018). Sulphide mineralization mainly occurs at the bases of these magmatic bodies, with few exceptions locating at the central to upper zones, such as the Huangshandong mafic body and the Tulaergen deposit.

Olivine-rich cumulates are the predominant host to the sulphides in the NW China deposits. Lherzolite and olivine websterite are the most prevalent rock types in the intrusions, such as the Tianyu and Baishiquan deposits in the Central Tianshan, Huangshandong, Huangshanxi, Huangshannan, Xiangshanzhong, Tudun, Tulaergen, and Hulu deposits in the Eastern Tianshan. Dunite is one of the main rock types of the intrusions from the Beishan, such as the Poyi and Poshi intrusions (Xue et al., 2016). The Kalatongke deposit comprises 14 small mafic intrusions, with the orebodies mostly hosted by the Y1 and Y2 intrusion. Olivine grains are common in the Y1 intrusion, where olivine norite is the main rock type, but rarely found in the others. (Zhang et al., 2009; Gao and Zhou, 2013; Mao et al., 2021). The olivine from the NW China deposits has variable Fo values (from 70 to 90 mol%) (Figure 7). Generally, the Ni content in olivine decreases with decreasing Fo value (Figure 7), as expected for simple fractional crystallization. For each deposit, the Ni variation cannot be adequately produced by fractional crystallization alone. For instance, the Poyi olivines show wide Ni variation (from 1500 to 3500 ppm) but subtle Fo variation (88-89 mol%).

The intrusions of this province show no clear discrimination on the basis of olivine chemistry between mineralized and weakly or unmineralized intrusions (Figure 7). The mineralized Huangshanxi intrusion shows a wide range in Ni, 400-1750 ppm, over a restricted range in Fo, but similar ranges are seen in unmineralized and weakly mineralized bodies also. Huangshandong contains both Ni-depleted and Ni-enriched olivine at relatively low Fo contents, whereas Kalatongke shows a grouping of relatively Ni-enriched olivines at around Fo75 compared with the rest of the CAOB data set, although less enriched than the olivines at Savannah (Figure 6). Notably, these Kalatongke samples are primarily sulfide-bearing orthocumulates, whereas the more Fo-rich samples from Poyi and others are adcumulate to mesocumulates. Huangshannan stands out as having strongly Ni-enriched olivines relative to the rest of the province, and to orogenic-setting intrusions generally, over a range of Fo contents. The distinctive character of the Huangshannan and Kalatongke olivines may be related to trapped liquid effects, as discussed below. With reference to

the modelled sulfide-free olivine (MSFM) field, distinct depletion is seen in Tulaergen (most samples), Huangshanxi, Hunangshandong, Honqiling, Xiarihamu, and Poyi.

Also included in this comparison is the Xiarihamu deposit, a small ultramafic-dominated intrusion of Paleozoic age in the East Kunlun orogenic belt in Tibet, containing a large accumulation of disseminated sulfides (Li et al., 2015; Song et al., 2016; Song et al., 2020), entirely unrelated to the CAOB suite. It is marked by a very wide range of Ni contents at a relatively high and narrow range of Fo contents, similar to Poyi.

As in the previous section for the Savannah area intrusions, sufficient data are available to subdivide individual samples on their sulfide content (Figure 7B). Depletion signals are present in sulfide-free as well as sulfide-bearing samples from the same intrusion (e.g. Poyi, Honqiling), although Ni-enriched olivines (Kalatongke and Huangshandong) tend to be restricted to sulfide-bearing samples. This can be taken as evidence for Ni enrichment being due to trapped liquid equilibration effects, discussed further below.

Figure 7.

Proterozoic orogenic belt: the Svecofennian (Raahe-Ladoga) Orogenic Belt, Finland. The Svecofennian Orogenic Belt (also known as the Raahe-Ladoga Belt, or the Kotalahti Nickel Belt) is a Paleoproterozoic (1.88 Ga) belt of polydeformed gneisses and amphibolites extending through central Finland (Makkonen et al., 2008; Makkonen, 2015). It is co-eval and probably correlative with the Vammala Nickel Belt in the south west of Finland. The belt contains over a dozen distinct mafic and mafic-ultramafic intrusions, several of which – Rytky, Kotalahti, Hitura and Enankoski – contain mined or subeconomic Ni-Cu sulfide deposits (Makkonen et al., 2008; Makkonen, 2015), along with a suite of mafic metavolcanic rocks at least some of which are considered to be co-magmatic with these intrusions (Barnes et al., 2009). Most of these intrusions are deformed and in some cases dismembered and are considered to have been emplaced during the peak of metamorphism in the belt (Makkonen et al., 2015). The weakly differentiated, dominantly ultramafic Vammala-type intrusions consist almost entirely of olivine cumulates and represent magma conduits. The more strongly differentiated, mafic and mafic–ultramafic, Kotalahti type intrusions consist of olivine cumulates, pyroxene cumulates, and plagioclase-bearing cumulates. The parental magma was basaltic with MgO contents mostly around 10–12 wt%. The mineralized intrusions show chemical evidence for crustal contamination. Makkonen et al. (2008) identified Ni-depleted olivine in the mineralized intrusions. Some of the mineralized intrusions contain complexly zoned cumulus and poikilitic pyroxenes, features not observed in similar rock types from the unmineralized bodies (Schoneveld et al., 2020).

A new compilation of olivine data drawing on Makkonen et al. (2008) and Lamberg (2005) is shown in Figure 8. There is no clear-cut discrimination between the mineralized and barren intrusions, but some indicative features are present. Distinct depletion is evident at low Fo contents in the weakly mineralized Ylivieska intrusion; the mineralized Rytky intrusion shows a wide range in Ni from 600 to 2400 ppm for a restricted range of 81-84 mol % Fo; the Nirimaki intrusion shows a similar trend to Rytky but displaced to lower Fo; and the weakly mineralized Laukukangas body shows a grouping of high-Ni, low Fo olivine similar to those seen at Kalatongke in the CAOB (Figure 7). Data for several of the intrusions (Luusniemi, Ylivieska, Heimonvouri) fall to the lower Ni end of the range of Ni in this tectonic setting, and well below the data cloud for plume-related settings.

Figure 8.

Ural-Alaskan Complexes. Ural-Alaskan Complexes are a rare but widely distributed component of orogenic belts in the Phanerozoic and Proterozoic, and in some cases contain sub-economic Ni-Cu sulfide mineralization, usually in the form of disseminated sulfides (Thakurta et al., 2008). Examples of this are the Duke Island Intrusion in Alaska (Li et al., 2013; Thakurta et al., 2014) and the Turnagain Complex in British Columbia (Clark, 1980). Olivine data from these intrusions are compared with the data contours on barren orogenic belt intrusions in Figure 9. Duke Island and some samples from Turnagain, along with the Akarem Complex in Egypt, which also contains disseminated mineralization (Helmy and Mogessie, 2001) contain distinctly Ni-depleted olivines falling well below the reference field and showing wide variability in Ni for limited Fo.

Figure 9.

The Kevitsa intrusion, Finland. The 2.058 Ga Kevitsa intrusion (Mutanen, 1997; Santaguida et al., 2015; Luolavirta et al., 2017; Luolavirta et al., 2018) is located in the Central Lapland greenstone belt in northern Finland. It is part of a suite of small to medium sized mafic-ultramafic intrusions, including the large Koitelainen layered intrusion as well as the neighbouring Sakatti intrusion hosting the Cu-Ni Sakatti deposit. These intrusions range in age from 2.1 Ga to 1.8 Ga (Huhma et al., 2013). They are emplaced into a volcanic suite containing komatiites. The Kevitsa intrusion occupies a surface area of approximately 16 km^2 and consists of a lower ultramafic unit up to 2 km in thickness, overlain by a mafic unit over several hundred metres thick. The ultramafic unit is composed of interlayered olivine pyroxenite and websterite, with local development of cyclic units, but for the most part lacking obvious internal layering (Santaguida et al., 2015), but showing inward-dipping cryptic layering defined by variations in the sulfide tenors (Le Vaillant et al., 2017). The Kevitsa Ni-Cu-(PGE) deposit occurs in the middle part of the ultramafic unit, associated with variably layered olivine pyroxenites and websterites. The deposit consists entirely of disseminated sulfides with widely varying Ni, Cu and PGE tenors, with a published combined resource of 237 Mt at 0.28% Ni,

0.41% Cu and 0.6 ppm 3E (Pt + Pd + Au) (Geological Survey of Finland website, 2016) with Ni grades up to around 0.6% (99th percentile on all assays in the database). The mineralization has been separated into different ore types, mainly on the basis of their Ni-PGE tenors showing a broadly layered distribution with higher tenors generally at higher levels within the stratigraphy (Le Vaillant et al., 2017). Low tenor disseminated but locally net-textured ores form near the base of the intrusion and along the margins of the Cu-Ni mineralization are classified as ‘‘false ore”. This pyrrhotite-rich mineralization has Ni tenors less than 1% and is typically associated with abundant country rock xenoliths. The ‘‘regular” or “normal” ore represents the bulk (>90%) of the economic resource and is characterized by 2–6 vol% of sulfides (pyrrhotite, pentlandite, and chalcopyrite) and average Ni and Cu ore-grades of 0.3 and 0.4 wt% respectively (Santaguida et al., 2015) with a range of Ni tenors between 1 and 10 % and PGE tenors between about 1 and 5 ppm. The volumetrically minor ‘‘Ni–PGE ore” has a similar sulfide content to that of the Normal ore, but the sulfides are predominantly pentlandite, pyrite and millerite. These ores have higher and more variable Ni grades, lower Cu grades (Ni/Cu = 1.5–15), and extreme Ni tenors ranging as high as 30%, attributed to high R factors in olivine-rich suspensions (Barnes et al., 2013a) with a likely, possibly assimilated komatiitic component (Yang et al., 2013). Pockets of Ni-PGE ore are developed throughout the orebody but the main development is in the upper part of the section (Le Vaillant et al., 2017).

The Kevitsa occurrence provides a useful case study in the variability of olivine compositions (Figure 10) within a single extensively mineralized intrusion that shows a wide range in nickel tenors. The most striking feature of the dataset is the presence of a group of ultra-Ni-rich olivines within the Ni-PGE ores (Yang et al., 2013), but the dataset is also characterized by strongly Ni-depleted olivines associated with the very low Ni-tenor False Ores (Luolavirta et al., 2017). The False Ores are interpreted to be the opposite case to the Ni-PGE rich ores: the result of very restricted equilibration between abundant assimilated sulfide and a poorly-stirred, high viscosity crystal mush (Le Vaillant et al., 2017), or alternatively as the result of extensive pre-emplacement fractional extraction of sulfide (Luolavirta et al., 2018). Within the strongly Ni-enriched part of the data set, distinct linear arrays are developed at sample scale where Ni correlates negatively with Fo (Figure 10B): this is a hallmark of sample-scale trapped liquid equilibration, as discussed further below.

Figure 10.

Nova-Bollinger. The Mesoproterozoic Nova – Bollinger Ni-Cu – sulfide ore deposit is located in the Albany-Fraser Orogen in Western Australia (Maier et al., 2016). The host-rocks are mafic - ultramafic intrusive cumulates subdivided into two connected intrusions, designated Upper and Lower (Figure 11). The Upper Intrusion is bowl-shaped and modally layered with alternating peridotite and norite mesocumulate layers, with a basal series of dominantly orthocumulate mafic lithologies. The Lower

is a much thinner semi-conformable chonolith (flattened tube-shaped intrusion) comprising mostly unlayered mafic to ultramafic orthocumulates (Taranovic et al., 2021). The Lower Intrusion hosts all the high-grade mineralization and most of the disseminated ores. A distinctive plagioclase-bearing lherzolite containing both orthopyroxene and olivine as cumulus phases is a characteristic of the Lower Intrusion and the basal series of the Upper. The intrusions were emplaced under peak metamorphic conditions at around 20-25 km depth into granulite facies paragneisses which underwent partial melting during extensive infiltration of sulfides into the footwall (Barnes et al., 2020). The geometry of the intrusions and the disposition of the sulfides suggest that the Lower intrusion formed as an apophysis off the base of the Upper, propagating westward into the footwall rocks (Taranovic et al., 2021). Nova-Bollinger ores contain Ni tenors in the 5-9% range (Barnes et al., 2021).

Figure 11.

A wide spread of Ni and Fo contents is present. The most Ni-depleted Fo rich olivines are located within the upper part of the Upper Intrusion, and also within the Lower intrusion where the two intrusions diverge. Less Fo rich olivines with trends towards Ni enrichment are in the Lower (ore-bearing) intrusion (Figure 11). The Lower Intrusion rocks are distinctly more orthocumulate such that the trend towards lower Fo and higher Ni can be attributed to trapped liquid effects, as discussed further below. This is particularly clear in the purple diamond symbols in Figure 11A. However, the most significant feature of the Nova data set is the presence of a widespread group of low-Ni, high-Fo samples located predominantly in the Upper Intrusion, and particularly in the entirely unmineralized layered ultramafic cumulates higher in the sequence (Figure 11B). This is significant from an exploration viewpoint in that the Lower Intrusion is entirely blind to the surface; recognition of Ni depletion in these ostensibly barren upper cumulate layers would be a pathfinder to the orebodies.

The choice of baseline for Nova is problematic. While the setting is undoubtedly a convergent margin orogenic belt (Spaggiari et al., 2015), the Fraser Zone magmatic complex to which Nova belongs is a large volume mafic suite with a restricted age range and trace element characteristics that could be interpreted as plume-like, indicative of a LIP affinity (Taranovic et al., 2021). If the Fraser Zone is indeed a LIP, then the low-Ni, high Fo olivines of the Upper intrusion are definitively depleted. Regardless, the Ni in olivine signal of the Nova-Bollinger intrusions is clearly positive for mineralization.

Discussion: controls on olivine Fo-Ni variations in sulfide-bearing magmatic systems

As we have seen, intrusion-hosted olivines show wide and complex variability in Ni-Fo trends, even within the same intrusion, indicating that sulfide melt equilibration is only one of a number of factors influencing the Ni content of olivine. Some of these factors are considered and modelled in the following section.

Range of variability of Ni in carrier magmas

The silicate magmas that form magmatic sulfide ores (carrier magmas) are known to have a wide range of Ni contents, from ~1600 ppm in primitive komatiites to ~100 ppm in some mafic-hosted systems (Barnes et al., 2016). The ability of relatively low-Ni mafic magmas to form deposits with economic Ni contents arises from the very high partition coefficient D_{Ni} of Ni between sulfide and olivine; this D_{Ni} value increases strongly with falling temperature and hence is considerably higher in basalt than in komatiite (Kiseeva and Wood, 2015). The same effect applies to D_{Ni} between olivine and silicate melt (Li and Ripley, 2010; Matzen et al., 2013; Matzen et al., 2017a; Matzen et al., 2017b; Pu et al., 2021). The effect of this T dependence on olivine Ni contents gives rise to the observed wide variability in the Ni contents of primary mantle melts, (Li and Ripley, 2010; Yao et al., 2018) and basalt-hosted olivines (Sobolev et al., 2007; Herzberg et al., 2016), (Figure 1), a variability that could be further enhanced by variability in the pyroxene:olivine ratio in mantle sources (Sobolev et al., 2005). The presence of pyroxene-rich mantle-source regions has been proposed as a major controlling factor on the range of olivine compositions in various Chinese deposits (Song et al., 2011b; Song et al., 2011c; Lu et al., 2019), but remains a hotly debated topic beyond the scope of this contribution.

We have carried out a series of model calculations on compositions of potential carrier magmas and associated olivines generated at a variety of depths and primary water contents and undergoing fractional crystallization, following the methods of Yao et al. (2018). A representative series of these curves are shown in Figure 12, for conditions corresponding to sulfide undersaturation (i.e. no sulfide liquid involved during melting or fractional crystallization) and appropriate values for the crystallization pressure (1 kbar), water content (1 wt% H_2O) and oxygen fugacity (QFM-1). The emplacement depths of most these mafic-ultramafic intrusions are probably shallow, resulting in a relatively narrow pressure range varying from 0.5 to 2.5 kbar (Norilsk, (Yao and Mungall, 2021); Bushveld, (Maier et al., 2013)), which has little influence on the trendlines of Ni in the crystallized olivine grains (Appendix Fig. A1-a). The addition of water into the parental magma will decrease the olivine saturation temperature and enhance the olivine stability during crystallization (dropping to a

lower Fo number), but the partition coefficient of Ni between olivine and melt has been shown to have a negligible dependence on water content (Pu et al., 2021). The combined effects of water content on the Ni trendlines of olivine grains is confirmed to be slight when the initial H_2O in the parent magma varies from 0 to 3 wt% (Appendix Fig. A1B). The oxygen fugacity of plume-associated magmatism may mostly vary from QFM-2 to QFM, while the parental magma derived by flux-melting of mantle wedge can have a higher oxygen fugacity that can even reach QFM+2. These most oxidized conditions are within the range where most of the S in the magma would be dissolved as S^{6+} rather than S^{2-} such that sulfide formation is inhibited (Jugo et al., 2005), so can be disregarded in this context. In both settings, for fO_2 below QFM+1, the variation of fO_2 simply drives a limited horizontal movement of the trendlines of Ni contents (Appendix Fig. A1C, D) because a higher fO_2 results in the increase of Fe^{3+}/Fe^{2+} in melt, which further elevates the Fo content of olivine. Hence, the variations of crystallization conditions have only a limited impact on the modelled Ni trendlines. The reader is referred to Appendix 1 for more detailed discussion of the modelling.

These curves are used to define a range for model olivine compositions that can be derived from plausible mantle partial melts, taking the upper limit as the uppermost plume model curve at any Fo and the lower as the 10% partial melt in the depleted MORB mantle (DMM) flux model. This range is plotted as a reference field on the data plots shown above.

Aside from this reference field, the main conclusions from the modelling are

1. the curve for olivine fractionation in plume magmas changes over a factor of about 50% (2400 to 3600 ppm) between pyroxenite-free and 30% pyroxenite sources, but converges to similar values with fractionation. The range between sources gives model trends that match reasonably well with the CLIP basalt data array, but fall to the low end compared with intrusion-hosted olivines.
2. Models involving flux melting from hydrated depleted mantle generate lower Ni in olivine for the same Fo, but also (probably for the same reason) fall at the lower Ni side of the field for intrusion hosted olivines. Natural olivines from convergent margin lavas show a wide spread of Ni at high Fo contents.

Figure 12

The consistent difference between olivine Ni contents in LIP relative to orogenic belt settings above probably arises largely from these primary controls on the compositions of the carrier magmas. More generally, it provides a major confounding effect on the ability to discern sulfide extraction history in magma suites from olivine compositions alone, reinforcing the need to use different baselines when comparing LIP settings with convergent margin settings.

Fractional crystallization of olivine + sulfide liquid

In most models of olivine evolution in sulfide-saturated systems, sulfide is assumed to be segregated from the carried magma along with the fractional crystallization of olivine in some defined proportion. In the models shown in Figure 13, olivine compositions are shown for fractional crystallization of two starting liquids: a plume melt including a 50% contribution from a "pyroxenite" mantle corresponding to the uppermost curve in Figure 12A, and from a melt generated by flux melting of depleted mantle (Figure 12B) as the proportion ratios of olivine and sulfide in each crystallization increment are assumed as 50, 100, 200 and 500. The partition coefficient of Ni between sulfide and melt is from the formulation of Kiseeva and Wood (2015). As expected, variation in the proportion of olivine to sulfide from 50 to 500 produces a change over a factor of 4-5 in Ni in olivine. Various estimates of the proportion of sulfide to olivine under cotectic conditions (i.e. fractionation of olivine plus sulfide liquid exactly along the sulfide saturation surface) have been made, using various parameterizations of the sulfide content at sulfide liquid saturation (SCSS) as a function of melt chemistry and temperature (Ariskin and Barmina, 1999; Li and Ripley, 2005; Barnes, 2007; Ariskin et al., 2013; Godel et al., 2013) with a general consensus of values around 100-200 for olivine saturated magmas. Hence cotectic fractionation should result in Ni depletion by factors of around 3-4.

Figure 13

Recharge and magma mixing

Recharge and magma mixing of derivative fractionated magmas with primitive parental magmas has been identified in MORBs and other mafic suites and has been proposed by Gleeson and Gibson (2019) as a mechanism for generating anomalous Ni enrichment in olivine. This follows from the convex-upward form of curves for Ni vs Fo in olivine during fractional crystallization (Figure 12, Figure 13). This type of process may account for otherwise unexplained Ni-enriched olivine trends such as in the Gudchichinsky Picrites of the Siberian LIP (Figure 1A), and also the high Ni in Hawaiian picrite olivines reported by Sobolev et al. (2007). Where magmatic sulfides are generated within multiply recharged sill-dyke networks, as proposed by Barnes et al. (2016), this process has good potential to obscure Ni depletion signals and indeed to generate enrichment. Presence of sulfide in the system may enhance this tendency, as discussed further below.

Gleeson and Gibson (2019) point out that recharge and mixing provides a viable alternative hypothesis to the "pyroxenite source" model, which has been involved for some Ni deposits and camps, notably several of the Chinese deposits (Lu et al., 2019). Numerous other studies (Matzen et al., 2017b; Yao et al., 2018) have pointed out other combinations of melting depth and mechanism

557 that avoid the need for pyroxenitic sources. Full discussion of this issue requires consideration of
558 trace elements and isotopic signals that are out of scope of this contribution, but we note that of the
559 deposits represented in this compilation, only a few (Mirabela, Poyi, Xiarihamu, Eagle and Kevitsa)
560 contain olivines in the high Fo (>85 mol pct) and high Ni (>3000) ppm that are claimed by Sobolev et
561 al (2007) as evidence for pyroxenitic mantle sources.

562 ## R factor effects

563 The term "R-factor" refers to the widely used equation (Campbell and Naldrett, 1979) describing the
564 composition of silicate and sulfide melt during closed-system batch equilibration, where R is defined
565 as the mass ratio of silicate to silicate liquid at equilibrium during a closed-system batch
566 equilibration event. The equation can readily be adapted to also include olivine as a third component
567 in the reaction (Barnes et al., 2013a). It is particularly applicable to the situation where a sulfide
568 xenomelt (Lesher, 2017) is incorporated into a magma body by assimilation of crustal rocks and
569 equilibrates with a fixed mass of magma. Olivine and sulfide compositions can be modelled by a one-
570 stage three-way batch equilibrium calculation, involving equilibrium between olivine, sulfide liquid
571 and silicate liquid using experimental values for partition and distribution coefficients (Barnes et al.,
572 2013a). Figure 14 shows the results of these calculations for variable R and four hypothetical silicate
573 melt compositions (Table 1): komatiite ("kom"), a high-Mg plume basalt ("Plume bas 18"), a
574 ferropicrite and a MORB, using typical values taken from data compilations of Barnes and Fiorentini
575 (2012) and Barnes et al. (2015). The main conclusion from the model results in Figure 14 is that
576 much of the spread of Fo and Ni concentrations in olivine found between individual deposits can
577 theoretically be explained by the combination of initial melt composition and R factor. Variations in
578 R within a single deposit, as for example in the Kevitsa intrusion noted above, can generate the
579 observed spread in olivine Ni for a limited range of Fo, and this variability would be expected to
580 correlate with sulfide tenor, as indeed it does at Kevitsa. The prime cause of strongly Ni depleted
581 olivine is equilibration with silicate and sulfide liquid at low R values, a process which generates
582 correspondingly low-Ni tenor sulfides, as seen in the Kabanga example above (Figure 5) and
583 modelled in Figure 14.

584 It is commonly concluded that depletion of Ni in olivine necessarily implies that the silicate
585 component has been depleted by some previous "upstream" sulfide extraction event prior to the
586 crystallization of the assemblage being studied; i.e. that the depletion implies the existence of an
587 additional sulfide body or bodies elsewhere in the intrusion network. Figure 14 shows that this is not
588 a necessary conclusion: a single stage batch equilibration event can produce a wide range in degrees
589 of Ni depletion depending on the R factor. Low R factor, low Ni-tenor sulfide necessarily coexists
590 with low-Ni olivine at equilibrium.

Figure 14.

Table 1.

Trapped liquid effects

One of the factors affecting cumulus mineral compositions is the effect of equilibration between olivine and trapped intercumulus liquid (Barnes, 1986). The principle is illustrated in Figure 15. The original orthocumulate consists of a mixture of olivine, sulfide and silicate liquid, assumed to be in equilibrium (Figure 15A), with the composition of the three phases determined by the three-way equilibration at a given R factor (mass ratio of silicate to sulfide) and proportion of silicate to olivine (F). In the illustrative calculations shown here, the proportion of olivine participating in this initial bulk equilibrium is assumed to be small, 5%. Olivine and sulfide then accumulated mechanically in different proportions along with a component of trapped interstitial silicate melt to form a partially solid mush (Figure 15B). For simplicity we assume that the resulting component has 40% trapped liquid and 5% sulfide (at and above this proportion of sulfide, the change in composition of sulfide during the trapped liquid reaction is minor). As the olivine then re-equilibrates with the evolving trapped liquid during solidification (Figure 15C), it becomes more Fe-rich, and consequently is constrained to also become more Ni rich due to the exchange reaction

NiO (olivine) + FeS (sulfide) = NiS (sulfide) + FeO (olivine) (1)

The distribution coefficient for this reaction K_D is given by

$$K_D = (X_{NiS}/X_{FeS})_{\text{sulfide liquid}}/(X_{NiO}/X_{FeO})_{\text{olivine}}, \quad (2)$$

which has a value independent of temperature but dependent on fO_2 and the sulfide composition (Brenan 2003; Barnes et al., 2013a; Mao et al., 2017).

The sulfide is the dominant reservoir of Ni in the rock for abundances of more than about 5%, such that its composition is only slightly affected by the trapped liquid reaction. Consequently, as the FeO content of the olivine increases, the NiO content must also increase to satisfy the K_D. This gives rise to a negative correlation between Fo and Ni, first recognized in the JM Reef of the Stillwater Complex (Barnes and Naldrett, 1985) and identified subsequently at Voisey's Bay (Li and Naldrett, 1999). Hints of such correlations are present in several of the data sets presented in this study, notably Kevitsa (Figure 10).

Figure 15.

The effect has been quantified for a variety of different starting compositions and assumptions (Figure 16), using an iterative solution method based on that of Barnes et al. (2013a). The calculation

procedure involves (1) calculation of olivine, sulfide and liquid compositions for each starting liquid (Table 1) as a function of silicate:sulfide mass ratio R, corresponding to stage A in Figure 15; and (2) calculation of new olivine and sulfide composition following complete equilibrium crystallization of a mixture of 55% olivine, 5% sulfide and 40% trapped silicate liquid (Figure 15 b-c).

Figure 16.

The calculation shows that trapped liquid reaction can have a significant effect on Ni content of olivine, most evident in sulfide-bearing orthocumulates where the change in olivine Fo content is greatest. For komatiites, the effect is enhanced by the composition dependence of the K_D on the Ni content of the sulfide, which becomes a significant factor where the Ni content of the sulfide is in the 20-30% Ni range (Barnes et al., 2013a), but it is present for all assumptions about parent melts. The range of Ni variation is comparable to that produced by changes in R over factors of up to an order of magnitude.

Sulfide "cannibalization" and Ni enrichment

It is likely that the trapped liquid effect contributes considerably to the "noise" in the data and may well explain the observation of anomalously Ni rich olivines in some deposits such as Kalatongke, Savannah, Nova-Bollinger and Kevitsa. However, in a number of cases high Ni is not specifically associated with sulfide-bearing orthocumulates so another explanation is called for.

The sequence of events may be more complex than the simple scenario modelled in Figure 16. For example, fluid dynamic considerations predict that pools of Ni-enriched magmatic sulfide liquid may commonly be "cannibalized" and entrained as droplets in a flowing slurry of silicate magma, liquid sulfide and olivine (Barnes and Robertson, 2019; Lesher, 2019). In this case (Figure 17), we have a starting scenario similar to Figure 15A, except that rather than starting out as a Ni-free Fe-sulfide xenomelt, the sulfide component in the slurry is re-entrained magmatic sulfide that already has high Ni. For example, if the slurry has 5% of sulfide with 10% Ni, 5% olivine with 0.1 % Ni and the silicate melt has 250 ppm Ni (realistic assumptions for a typical mafic-hosted deposit), the sulfide component contains 95% of the total Ni budget and will effectively buffer the Ni contents of both silicate melt and olivine. In contrast, the silicate melt is the predominant reservoir of Fe and Mg and buffers the olivine Fo content. Where this olivine is relatively Fe-rich, the Fe-Ni exchange reaction will cause it to gain Ni from the re-entrained sulfide, without greatly affecting the Ni content of that sulfide component. In a more extreme case, where the sulfide has 30% Ni (towards the upper end of sulfides associated with komatiites), an olivine with an initial composition of Fo84 would react towards a Ni content in excess of 10,000 ppm for a typical Ni/Fe K_D of around 8, provided that equilibrium was attained between the three phases during flow. Further trapped liquid reaction

post-deposition could then push this value even higher, to the extreme values of 10,000-15,000 ppm Ni seen in the Ni-PGE ores at Kevitsa. The effect is further amplified as the K_D value increases with increasing Ni in the sulfide. This is consistent with the suggestion of Yang et al. (2013) that these unusual ores could be the result of assimilation of komatiite-derived sulfide, and with the explanation offered by Burnham et al. (2003) for anomalously Ni-rich olivines in the komatiite-associated William Lake intrusion in the Thompson Nickel Belt, Manitoba (Burnham et al., 2003). More generally, the process of re-entrainment of pre-formed magmatic sulfide by magma-olivine mixtures with variable composition could explain the apparent paradox that several deposits mentioned above, and also Ntaka Hill (Barnes et al., 2019) and William Lake, show signals of Ni enrichment rather than depletion in olivine. In particular the presence of a strong Ni enrichment signal in sulfide-free rocks in the Savannah intrusion (Figure 6B) is attributed to this effect. (It is also possible that the same effect could operate in reverse: an Mg-rich olivine reacting with sulfide formed initially in equilibrium with a relatively Mg-poor olivine could have its Ni content reduced).

Figure 17.

Multi-stage emplacement and sulfide re-entrainment in predominantly vertical sill-dyke-conduit complexes (Barnes et al., 2016) could provide an additional set of confounding factors for the interpretation of Ni in olivine data. On a more positive note, the presence of anomalously Ni-enriched olivines within a suite of otherwise similar intrusions may be as much of a positive indicator for mineralization as depletion.

Summary of sources of variation of Ni in olivine.

Multiple sources of variance in Ni content of olivine at given Fo content could be operative at multiple stages in the formation of a mineral system. Some of these processes are summarized on Figure 18.

- Variability in mantle melt composition due to depth, water content (and possibly source). Baselines for Ni in olivine in relation to Fo content are somewhat lower in orogenic belt settings relative to intrusions in continental LIPs. This is probably related to differences in initial parent magma compositions, with plume magmas generally forming deeper and at higher temperatures (Yao et al., 2018).
- Subsequent fractional crystallization with and without sulfide (Figure 18);
- Recharge and magma mixing (Gleeson and Gibson, 2019) (Figure 18);.
- Batch equilibration between olivine and sulfide at variable R and olivine/liquid ratio (Figure 14);

- Subsequent equilibration during trapped liquid crystallization in orthocumulates (Figure 18; Figure 15);
- Reaction of olivine with sulfide during “cannibalization”/re-entrainment; olivine could become anomalously enriched or depleted during such events depending on the sequence of emplacement and relative change in melt composition and olivine Fo content.

Figure 18.

Implications and application to exploration

While there is no clear, universal discrimination evident in Ni in olivine between ore-bearing, weakly mineralized and barren intrusions in either CLIP or orogenic categories, sulfide-related signals of both enrichment and depletion can be detected at intrusion scale in many cases, in both sulfide-bearing and sulfide-free samples. Low-R factor, low-tenor sulfides are associated with low-Ni olivines in a number of examples such as Kabanga, and these cases stand out clearly; to put it another way, Ni depletion is a very effective tool for finding low tenor deposits. A lack of clear mineralized/barren distinction in specific groups of related intrusions, e.g. the deposits of NW China or the Kotalahti Belt in Finland, may well be due to “false negatives” where undiscovered mineralization exists in specific intrusions or in their feeder systems, or may also be due to a multiplicity of confounding factors as summarized in Figure 18. In these cases, wide variability of high and low Ni at similar Fo may be more useful as a fertility indicator than simple depletion signals. Wide variability of both Fo and Ni between related intrusions at regional scale may be a useful regional prospectivity indicator, more than an intrusion-scale discriminant. Anomalously high Ni in sulfide-free samples may in some cases be an indicator of prospectivity. In general, the use of Ni-olivine as a fertility tool is more likely to generate false negatives than false positives, but both are possible, and the technique should be used as part of a broader weight-of-evidence approach.

The increasing availability of laser ablation – ICPMS trace element data potentially opens new opportunities for practical applications. A small number of existing data sets, e.g. from Savannah (Le Vaillant et al., 2020) and Nova (Taranovic et al., 2021), show that the presence of positive correlations between Ni and Co in olivine may be a useful indicator of reaction with sulfide, and further work is warranted to test this association.

More broadly, Ni in olivine is certainly informative as a petrogenetic process indicator in magmatic sulfide mineral systems. The question of whether “pyroxenite” components in plume sources contribute to higher Ni olivines remains open and, given the large number of confounding variables, is probably not resolvable on olivine data alone.

Acknowledgments

We thank Yiguan Liu for assistance with data compilation. Data for the Halls Creek Orogen and for the Nova-Bollinger system were collected within industry funded projects supported by Panoramic Resources and IGO Ltd respectively. Louise Schoneveld provided a helpful review of a preliminary draft, and we are grateful to American Mineralogist reviewers James Brenan, Chusi Li and Huan Chen for constructive suggestions.

Appendices/Supplementary

Supplementary Table 1. Data source table and references.

Appendix 1. Modelling methods

Mafic-ultramafic magmas in continental LIPs are derived from decompression melting of mantle beneath the rigid lithosphere. The geochemical characteristics of these mantle-derived magmas are mostly dependent on geochemical features, mineralogy and potential temperature) of the mantle source, as well as the melting degree which is determined by the thickness of lithosphere because the upwelling of mantle ceases at the base of rigid lithosphere. Given that the continental lithosphere is rarely thinned to below 80-100 km during the LIP event, the representative mantle-derived magma in the CLIP is adopted as the melt that is generated by the adiabatic decompression melting of the primary mantle (McDonough and Sun, 1995) with a hot potential temperature (1550 °C), and extracted from the source at 3 GPa (~100 km). This melt contains ~25 wt% MgO, 14 wt% FeO_t (total Fe expressed as FeO) and 1040 ppm Ni based on the model from Yao et al. (2018), and is used for a further model of fractional crystallization at the assumed condition. In order to account for the effect of mantle heterogeneity, this peridotite-derived melt is also mixed with the melt generated by a MORB-like pyroxenite mantle with the same decompression melting path (potential temperature, 1550 °C; terminal melting pressure, 3 GPa). The proportions of pyroxenite-derived melt in the mixed magmas are assumed as 10, 30 and 50%, respectively. The partition coefficient of Ni between the olivine and melt is calculated via the new equation that is calibrated on many 1-bar experiments spanning a wide range of melt and olivine compositions (Pu et al., 2017; Pu et al., 2021). The partition coefficients of Ni within the clinopyroxene-melt and orthopyroxene-melt pairs follow the equations from Matzen et al. (2017b). The olivine grains crystallized from the mixed magmas (especially contain 30-50% pyroxenite-derived melt) contain a higher Ni content than that of peridotite-derived melt at the high-Fo regime, but all modelled Ni trendlines become overlapped when the Fo value drops below 78 (Figure 12A). In general, the modelling results coincide with the

751 trends and distributions of CLIP olivine dataset (Fig. 12A) and can be considered as the baseline to
752 trace the influence of post-cumulus processes on the Ni content of olivines.

753 The petrogenesis of ultramafic-mafic intrusions in orogenic belts is extremely complex, and the
754 associated magmatism may be generated in subduction, collision and post-collision periods. Hence,
755 the partial melting process occurred in orogenic belt may involve the flux-melting of mantle wedge
756 during subduction, the upwelling of asthenosphere due to slab break off or lithospheric
757 delamination in syn- or post-collisional setting, and even the possible contributions of adiabatic
758 decompression melting of hot plume material. In the models presented here (Fig. A1), partial
759 melting processes in orogenic belt are simplified as the flux-melting of mantle wedge above the
760 subducted slab. The details of this melting model can be found in Yao et al. (2018). The mantle
761 source is simplified as the depleted MORB mantle (DMM) (Workman and Hart, 2005). We also set a
762 relatively high temperature (1300 °C) that is close to the anhydrous solidus of mantle wedge
763 peridotite at the crust-mantle boundary (~ 1 GPa), which corresponds to the subduction of a young
764 oceanic lithosphere with slow convergence rate and low subduction angle. The melting products
765 generated at different melting degree (5-25%) are adopted as the representative parental magmas
766 in orogenic belt to model the subsequent fractional crystallization at 1 kbar pressure. The melts
767 derived by flux-melting contain the relatively lower Ni contents (~245-273 ppm), and the melting
768 degrees here show a slight influence on the Ni trendlines of olivine (Figure 12B).

769 *Appendix Figure A1.*

References

Ariskin, A.A., and Barmina, G.S. (1999) An empirical model for the calculation of spinel-melt equilibria in mafic igneous systems at atmospheric pressure: 2. Fe-Ti oxides. Contributions to Mineralogy and Petrology, 134, 251- 263.

Ariskin, A.A., Danyushevsky, L.V., Bychkov, K.A., McNeill, A.W., Barmina, G.S., and Nikolaev, G.S. (2013) Modeling solubility of Fe-Ni sulfides in basaltic magmas: the effect of Ni in the melt. Economic Geology, 108.

Barnes, S.J. (1986) The effect of trapped liquid crystallization on cumulus mineral compositions in layered intrusions. Contributions to Mineralogy and Petrology, 93, 524-531.

Barnes, S.J. (2007) Cotectic precipitation of olivine and sulfide liquid from komatiite magma, and the origin of komatiite-hosted disseminated nickel sulfide mineralization at Mt Keith and Yakabindie, Western Australia. Economic Geology, 102, 299-304.

Barnes, S.J., Cruden, A.R., Arndt, N.T., and Saumur, B.M. (2016) The mineral system approach applied to magmatic Ni-Cu-PGE sulphide deposits. Ore Geology Reviews, 76, 296-316.

Barnes, S.J., and Fiorentini, M.L. (2012) Komatiite magmas and nickel sulfide deposits: a comparison of variably endowed Archean terranes. Economic Geology, 107, 755-780.

Barnes, S.J., Godel, B., Gürer, D., Brenan, J.M., Robertson, J., and Paterson, D. (2013a) Sulfide-olivine Fe-Ni exchange and the origin of anomalously Ni-rich magmatic sulfides. Economic Geology, 108, 1971-1982.

Barnes, S.J., Heggie, G.J., and Fiorentini, M.L. (2013b) Spatial variation in platinum group element concentrations in ore-bearing komatiite at the Long-Victor deposit, Kambalda Dome, Western Australia: enlarging the footprint of nickel sulfide orebodies. Economic Geology, 108, 913-933.

Barnes, S.J., Hill, R.E.T., Perring, C.S., and Dowling, S.E. (2004) Lithogeochemical exploration for komatiite-associated Ni-sulfide deposits: strategies and limitations. Mineralogy and Petrology, 82, 259-293.

Barnes, S.J., Makkonen, H.V., Dowling, S.E., Hill, R.E.T., and Peltonen, P. (2009) The 1.88 Ga Kotalahti and Vammala Nickel Belts, Finland: geochemistry of the mafic and ultramafic metavolcanic rocks. Bulletin of the Geological Society of Finland, 81, 103-141.

Barnes, S.J., Mole, D.R., Hornsey, R., and Schoneveld, L.E. (2019) Nickel-copper sulfide mineralization in the Ntaka Hill Ultramafic Complex, Nachingwea region, Tanzania. Economic Geology 114, 1135-1158.

Barnes, S.J., and Mungall, J.E. (2018) Blade shaped dykes and nickel sulfide deposits: a model for the emplacement of ore-bearing small intrusions. Economic Geology, 113, 789-798.

Barnes, S.J., Mungall, J.E., and Maier, W.D. (2015) Platinum group elements in mantle melts and mantle samples. Lithos, 232, 395-417.

Barnes, S.J., and Naldrett, A.J. (1985) Geochemistry of the JM (Howland) Reef of the Stillwater Complex, Minneapolis Adit area. I. Sulfide chemistry and sulfide-olivine equilibrium. Economic Geology, 80, 627-645.

Barnes, S.J., and Robertson, J.C. (2019) Time scales and length scales in magma flow pathways and the origin of magmatic Ni-Cu-PGE ore deposits. Geoscience Frontiers, 10, 77-87.

Barnes, S.J., Stanley, C.R., and Taranovic, V. (2021) Compositions and Ni-Cu-PGE tenors of Nova-Bollinger ores with implications for the origin of Pt anomalies in PGE-poor massive sulfides. Economic Geology, in press.

Barnes, S.J., Taranovic, V., Miller, J.M., Boyce, G., and Beresford, S.W. (2020) Sulfide emplacement and migration in the Nova-Bollinger Ni-Cu-Co deposit, Albany-Fraser Orogen, Western Australia. Economic Geology, 115, 1749-1776.

Brenan, J.M., (2003) Effects of fO2, fS2, temperature and melt composition on Fe-Ni exchange between olivine and sulfide liquid: implications for natural olivine-sulfide assemblages . Geochimica et Cosmochimica Acta, 64, 307-320.

Burnham, O.M., Halden, N., Layton-Matthews, D., Lesher, C.M., Liwanag, J., Heaman, L., Hulbert, L., Machado, N., Michalak, D., Pacey, M., Peck, D., Potrel, A., Theyer, P., Toope, K., and Zwanzig, H. (2003) Geology, Stratigraphy, Petrogenesis, and Metallogenesis of the Thompson Nickel Belt, Manitoba: Final Report for CAMIRO Project 97E-02, p. 410 pp. Mineral Exploration Research Centre, Sudbury.

Campbell, I.H., and Naldrett, A.J. (1979) The influence of silicate:sulphide ratios on the geochemistry of magmatic sulphides. Economic Geology, 74, 1503-1506.

Clark, T. (1980) Petrology of the Turnagain ultramafic complex, northwestern British Columbia. Canadian Journal of Earth Sciences = Revue Canadienne des Sciences de la Terre, 17(6), 744-757.

Deblond, A., and Tack, L. (1999) Main characteristics and review of mineral resources of the Kabanga-Musongati mafic-ultramafic alignment in Burundi. Journal of African Earth Sciences, 29, 313- 328.

Ding, X., Li, C., Ripley, E.M., Rossell, D., and Kamo, S. (2010) The Eagle and East Eagle sulfide ore-bearing mafic-ultramafic intrusions in the Midcontinent Rift System, upper Michigan: Geochronology and petrologic evolution. Geochemistry, Geophysics, Geosystems, 11(3).

Duchesne, J.-C., Liégeois, J.-P., Deblond, A., and Tack, L. (2004) Petrogenesis of the Kabanga-Musongati lay¬ered mafic-ultramafic intrusions in Burundi (Kibaran belt): Geochemical, Sr-Nd isotopic constraints and Cr-Ni behaviour. Journal of African Earth Sciences, 39, 133-145.

Duke, J.M. (1979) Computer simulation of the fractionation of olivine and sulfide from mafic and ultramafic magmas. Canadian Mineralogist, 76, 507-514.

Evans, D.M., Boadi, I., Byemelwa, L., Gilligan, J., Kabete, J., and Marcet, P. (2000) Kabanga magmatic nickel sulphide deposits, Tanzania: Morphology and geo¬chemistry of associated intrusions. Journal of African Earth Sciences, 97, 651-674.

Gao, J.-F., and Zhou, M.-F. (2013) Magma mixing in the genesis of the Kalatongke dioritic intrusion: Implications for the tectonic switch from subduction to post-collision, Chinese Altay, NW China. Lithos, 162, 236-250.

Gleeson, M.L.M., and Gibson, S.A. (2019) Crustal controls on apparent mantle pyroxenite signals in ocean-island basalts. Geology (Boulder), 47(4), 321-324.

Godel, B., Barnes, S.J., and Barnes, S.-J. (2013) Deposition mechanisms of magmatic sulphide liquids: evidence from high-resolution X-ray computed tomography and trace element chemistry of komatiite-hosted disseminated sulphides. Journal of Petrology, 54, 1455-1481.

Häkli, T.A. (1971) Silicate nickel and its application to the exploration of nickel ores. Bulletin of the Geological Society of Finland, 43, 247-263.

Hart, S.R., and Davis, K.E. (1978) Ni partitioning between olivine and silicate melt. Earth and Planetary Science Letters, 40, 203-219.

Helmy, H.M., and Mogessie, A. (2001) Gabbro Akarem, Eastern Desert, Egypt; Cu-Ni-PGE mineralization in a concentrically zoned mafic-ultramafic complex. Mineralium Deposita, 36(1), 58-71.

Herzberg, C., Vidito, C., and Starkey, N.A. (2016) Nickel-cobalt contents of olivine record origins of mantle peridotite and related rocks. The American Mineralogist, 101(9), 1952-1966.

Jesus, A., Mateus, A., Benoit, M., Tassinari, C., and Bento dos Santos, T. (2020) The timing of sulfide segregation in a Variscan synorogenic gabbroic layered intrusion (Beja, Portugal): Implications for Ni-Cu-PGE exploration in orogenic settings. Ore Geology Reviews.

Jugo, P.J., Luth, R.W., and Richards, J.P. (2005) Experimental data on the speciation of sulfur as a function of oxygen fugacity in basaltic melts. Geochimica et Cosmochimica Acta, 69(2), 497-503.

Kiseeva, E.S., and Wood, B.J. (2015) The effects of composition and temperature on chalcophile and lithophile element partitioning into magmatic sulphides. Earth and Planetary Science Letters, 424, 280-294.

870 Kohanpour, F., Gorczyk, W., Lindsay, M.D., and Occhipinti, S.A. (2017) Examining tectonic scenarios
871 using geodynamic numerical modelling: Halls Creek Orogen, Australia. Gondwana Research,
872 46, 95-113.
873 Lamberg, P. (2005) From genetic concepts to practice – lithogeochemical identification of Ni-Cu
874 mineralised intrusions and localization of the ore. Geological Survey of Finland Bulletin, 402,
875 1-266.
876 Le Vaillant, M., Barnes, S.J., Mole, D.R., Fiorentini, M.L., LaFlamme, C.K., Denyszyn, S., Austin, J.,
877 Patterson, B., Godel, B., Neaud, A., Hicks, J., Shaw-Stuart, A., and Mao, Y.J. (2020)
878 Multidisciplinary study of a complex magmatic system: The Savannah Ni-Cu-Co Camp,
879 Western Australia. Ore Geology Reviews, 117, 103292.
880 Le Vaillant, M., Fiorentini, M.L., and Barnes, S.J. (2016) Review of lithogeochemical exploration tools
881 for komatiite-hosted nickel sulphide deposits. Journal of Geochemical Exploration, 168, 1-19.
882 Le Vaillant, M., Hill, E.J., and Barnes, S.J. (2017) Simplifying drill-hole domains for 3D geochemical
883 modelling: an example from the Kevitsa Ni-Cu-(PGE) deposit. Ore Geology Reviews, 90, 388-
884 398.
885 Lehnert, K., Su, Y., Langmuir, C.H., Sarbas, B., and Nohl, U. (2000) A global geochemical database
886 structure for rocks. Geochemistry Geophysics Geosystems, 1, 1012.
887 Lesher, C.M. (2017) Roles of residues/skarns, xenoliths, xenocrysts, xenomelts, and xenovolatiles in
888 the genesis, transport, and localization of magmatic Fe-Ni-Cu-PGE sulfides and chromite. Ore
889 Geology Reviews, 90, 465-484.
890 Lesher, C.M. (2019) Up, down, or sideways: emplacement of magmatic Fe–Ni–Cu–PGE sulfide melts
891 in large igneous provinces. Canadian Journal of Earth Science, 56, 756-773.
892 Li, C., and Naldrett, A.J. (1999) Geology and petrology of the Voisey's Bay intrusion: reaction of
893 olivine with sulfide and silicate liquids. Lithos, 47, 1- 31.
894 Li, C., Naldrett, A.J., and Ripley, E.M. (2007) Controls on the Fo and Ni Contents of Olivine in Sulfide-
895 bearing Mafic/Ultramafic Intrusions: Principles, Modeling, and Examples from Voisey's Bay.
896 Earth Science Frontiers, 14, 177-183.
897 Li, C., Ripley, E.M., Thakurta, J., Stifter, E.C., and Liang, Q. (2013) Variations of olivine Fo-Ni contents
898 and highly chalcophile element abundances in arc ultramafic cumulates, southern Alaska.
899 Chemical Geology, 351, 15-28.
900 Li, C., Zhang, M., Fu, P., Qian, Z.Z., Hu, P., and Ripley, E.M. (2012) The Kalatongke magmatic Ni-Cu
901 deposits in the Central Asian Orogenic Belt, NW China: product of slab window magmatism?
902 Mineralium Deposita, 47(1-2), 51-67.
903 Li, C., Zhang, Z., Li, W., Wang, Y., Sun, T., and Ripley, E.M. (2015) Geochronology, petrology and Hf-S
904 isotope geochemistry of the newly-discovered Xiarihamu magmatic Ni-Cu sulfide deposit in
905 the Qinghai-Tibet Plateau, western China. Lithos (Oslo), 216-217, 224-240.
906 Li, C.S., and Ripley, E.M. (2005) Empirical equations to predict the sulfur content of mafic magmas at
907 sulfide saturation and applications to magmatic sulfide deposits. Mineralium Deposita, 40,
908 218-230.
909 Li, C.S., and Ripley, E.M. (2010) The relative effects of composition and temperature on olivine-liquid
910 Ni partitioning: Statistical deconvolution and implications for petrologic modeling. Chemical
911 Geology, 275(1-2), 99-104.
912 Lu, Y., Lesher, C.M., and Deng, J. (2019) Geochemistry and genesis of magmatic Ni-Cu-(PGE) and
913 PGE-(Cu)-(Ni) deposits in China. Ore Geology Reviews, 107, 863-887.
914 Luolavirta, K., Hanski, E., Maier, W., Lahaye, Y., O'Brien, H., and Santaguida, F. (2018) In situ
915 strontium and sulfur isotope investigation of the Ni-Cu-(PGE) sulfide ore-bearing Kevitsa
916 Intrusion, northern Finland. Mineralium Deposita, 53(7), 1019-1038.
917 Luolavirta, K., Hanski, E., Maier, W., and Santaguida, F. (2017) Whole-rock and mineral compositional
918 constraints on the magmatic evolution of the Ni-Cu-(PGE) sulfide ore-bearing Kevitsa
919 intrusion, northern Finland. Lithos, 296-299, 37-53.

Maier, W.D., Barnes, S.-J., and Groves, D.I. (2013) The Bushveld Complex, South Africa; formation of platinum-palladium, chrome- and vanadium-rich layers via hydrodynamic sorting of a mobilized cumulate slurry in a large, relatively slowly cooling, subsiding magma chamber. Mineralium Deposita, 48(1), 1-56.

Maier, W.D., Barnes, S.-J., and Ripley, E.M. (2011) The Kabanga Ni Sulfide Deposits, Tanzania: A Review of Ore-Forming Processes. Reviews in Economic Geology, 17, 217-234.

Maier, W.D., Barnes, S.J., Sarkar, A., Ripley, E.M., Li, C., and Livesey, T. (2010) The Kabanga Ni sulfide deposit, Tanzania: I. Geology, petrography, silicate rock geochemistry, and sulfur and oxygen isotopes. Mineralium Deposita, 45, 419-441.

Maier, W.D., Peltonen, P., and Livesey, T. (2007) The ages of the Kabanga north and Kapalagulu intrusions, western Tanzania: A reconnaissance study. Economic Geology, 102, 147-149.

Maier, W.D., Smithies, R.H., Spaggiari, C.V., Barnes, S.J., Kirkland, C.L., Yang, S., Lahaye, Y., Kiddie, O., and MacRae, C.M. (2016) Petrogenesis and Ni-Cu sulphide potential of mafic-ultramafic rocks in the Mesoproterozoic Fraser Zone within the Albany-Fraser Orogen, Western Australia. Precambrian Research, 281, 27-46.

Mäkitie, H., Data, G., Isabirye, E., Mänttäri, I., Huhma, H., Klausen, M.B., Pakkanen, L., and Virransalo, P. (2014) Petrology, geochronology and emplacement model of the giant 1.37 Ga arcuate Lake Victoria dyke swarm on the margin of a large igneous province in eastern Africa. Journal of African Earth Sciences, 97, 273– 296.

Makkonen, H.V. (2015) Nickel deposits of the 1.88 Ga Kotalahti and Vammala Belts. In W.D. Maier, R. Lahtinen, and H. O' Brien, Eds. Mineral Deposits of Finland, p. 253-287. Elsevier.

Makkonen, H.V., Makinen, J., and Kontoniemi, O. (2008) Geochemical discrimination between barren and mineralized intrusions in the Svecofennian (1.9 Ga) Kotalahti nickel belt, Finland. Ore Geology Reviews, 33(1), 101-114.

Mao, J.W., Pirajno, F., Zhang, Z.H., Chai, F.M., Wu, H., Chen, S.P., Cheng, L.S., Yang, J.M., and Zhang, C.Q. (2008) A review of the Cu-Ni sulphide deposits in the Chinese Tianshan and Altay orogens (Xinjiang Autonomous Region, NW China): Principal characteristics and ore-forming processes. Journal of Asian Earth Sciences, 32(2-4), 184-203.

Mao, Y.J., Barnes, S.J., Godel, B., Schoneveld, L.E., Qin, K.Z., Tang, D.M., Williams, M.J., and Kang, Z. (2021) Sulfide ore formation of the Kalatongke Ni-Cu deposit as illustrated by sulfide textures. Economic Geology, in revision.

Mao, Y.J., Qin, K.Z., Barnes, S.J., Ferraina, C., Iacono-Marziano, G., Verrall, M.R., Tang, D.M., and Xue, S.C. (2017) A revised oxygen barometry in sulfide-saturated magmas and application to the Permian magmatic Ni–Cu deposits in the southern Central Asian Orogenic Belt. Mineralium Deposita, 53, 731-755.

Matzen, A.K., Baker, M.B., Beckett, J.R., and Stolper, E.M. (2013) The temperature and pressure dependence of nickel partitioning between olivine and silicate melt. Journal of Petrology, 54, 2521-2545.

Matzen, A.K., Baker, M.B., Beckett, J.R., Wood, B.J., and Stolper, E.M. (2017a) The effect of liquid composition on the partitioning of Ni between olivine and silicate melt. Contributions to Mineralogy and Petrology, 172(1), 3.

Matzen, A.K., Wood, B.J., Baker, M.B., and Stolper, E.M. (2017b) The roles of pyroxenite and peridotite in the mantle sources of oceanic basalts. Nature Geoscience, 10(7), 530-535.

McDonough, W.F., and Sun, S.-S. (1995) The composition of the Earth. Chemical Geology, 120, 223-253.

Mole, D.R., Barnes, S.J., Le Vaillant, M., Martin, L.A.J., and Hick, J. (2018) Timing, geochemistry and tectonic setting of intrusion-hosted Ni-Cu sulfide deposits of the Halls Creek Orogen, Western Australia. Lithos, 314-315, 425-446.

Mutanen, T. (1997) Geology and ore petrology of the Akanvaara and Koitelainen mafic layered intrusions and the Keivitsa-Satovaaa layered complex, northern Finland. Bulletin of the Geological Survey of Finland, 395.

971 Naldrett, A.J., Duke, J.M., Lightfoot, P.C., and Thompson, J.F.H. (1984) Quantitative modelling of the
972 segregation of magmatic sulphides: an exploration guide. Canadian Institute of Mining and
973 Metallurgy Bulletin, 77, 46-56.
974 Pu, X., Lange, R.A., and Moore, G. (2017) A comparison of olivine-melt thermometers based on D
975 (sub Mg) and D (sub Ni) ; the effects of melt composition, temperature, and pressure with
976 applications to MORBs and hydrous arc basalts. American Mineralogist, 102(4), 750-765.
977 Pu, X., Moore, G.M., Lange, R.A., Touran, J.P., and Gagnon, J.E. (2021) Experimental evaluation of a
978 new H (sub 2) O-independent thermometer based on olivine-melt Ni partitioning at crustal
979 pressure. American Mineralogist, 106(2), 235-250.
980 Qin, K.-Z., Su, B.-X., Sakyi, P.A., Tang, D.M., Li, X.H., Sun, H., Xiao, Q.H., and Liu, P.P. (2011) Sims
981 zircon U-Pb geochronology and Sr-Nd isotopes of Ni-Cu-bearing mafic-ultramafic intrusions
982 in Eastern tianshan and Beishan in correlation with flood basalts in Tarim basin (NW china):
983 Constraints on a Ca. 280 Ma mantle plume. American Journal of Science, 311(3), 237-260.
984 Santaguida, F., Luolavirta, K., Lappalainen, M., Ylinen, J., Voipio, S., and Jones, S. (2015) The Kevitsa
985 Ni-Cu-PGE deposit in the Central Lapland Greenstone Belt in Finland. In W.D. Maier, R.
986 Lahtinen, and H. O' Brien, Eds. Mineral Deposits of Finland, p. 195-210. Elsevier.
987 Sarbas, B. (2008) The GEOROC database as part of a growing geoinformatics network. In S.R. Brady,
988 A.K. Sinha, and L.C. Gunderson, Eds. Geoinformatics 2008 - data to knowledge, Proceedings.
989 US Geological Survey Scientific Investigations Report 2008-5172, p. 42-43.
990 Savov, I.P., Ryan, J.G., D'Antonio, M., and Fryer, P. (2007) Shallow slab fluid release across and along
991 the Mariana arc-basin system; insights from geochemistry of serpentinized peridotites from
992 the Mariana fore arc. Journal of Geophysical Research, 112(B9), B09205.
993 Schoneveld, L.E., Barnes, S.J., Makkonen, H.V., Le Vaillant, M., Paterson, D.J., Taranovic, V., Wang, K.-
994 Y., and Mao, Y.-J. (2020) Zoned Pyroxenes as Prospectivity Indicators for Magmatic Ni-Cu
995 Sulfide Mineralization. Frontiers in Earth Science, 8(256).
996 Sobolev, A., Hoffman, A., Kuzmin, D., Yaxley, G., Arndt, N., Chung, S.-L., Danyushevsky, L., Elliott, T.,
997 Frey, F., Garcia, M., Gurenko, A., Kamenetsky, V., Kerr, A., Krivolutskaya, N., Matvienkov, V.,
998 Nikogosian, I., Rocholl, A., Sigurdson, I., Sushchevskaya, N., and Teklay, M. (2007) The
999 amount of recycled crust in sources of mantle-derived melts. Science, 316, 412-417.
1000 Sobolev, A.V., Hofmann, A.W., Sobolev, S.V., and Nikogosian, I.K. (2005) An olivine-free mantle
1001 source of Hawaiian shield basalts. Nature (London), 434(7033), 590.
1002 Song, X.-Y., Xie, W., Deng, Y.-F., Crawford, A.J., Zheng, W.-Q., Zhou, G.-F., Deng, G., Cheng, S.-L., and
1003 Li, J. (2011a) Slab break-off and the formation of Permian mafic–ultramafic intrusions in
1004 southern margin of Central Asian Orogenic Belt, Xinjiang, NW China. Lithos, 127(1–2), 128-
1005 143.
1006 Song, X., Wang, Y., and Chen, L. (2011b) Magmatic Ni-Cu-(PGE) deposits in magma plumbing
1007 systems; features, formation and exploration. Geoscience Frontiers, 2(3), 375-384.
1008 Song, X., Xie, W., Deng, Y., Crawford, A.J., Zheng, W., Zhou, G., Deng, G., Cheng, S., and Li, J. (2011c)
1009 Slab break-off and the formation of Permian mafic-ultramafic intrusions in southern margin
1010 of Central Asian orogenic belt, Xinjiang, NW China. Lithos (Oslo), 127(1-2), 128-143.
1011 Song, X., Yi, J., Chen, L., She, Y., Liu, C., Dang, X., Yang, Q., and Wu, S. (2016) The giant Xiarihamu Ni-
1012 Co sulfide deposit in the East Kunlun orogenic belt, northern Tibet Plateau, China. Economic
1013 Geology and the Bulletin of the Society of Economic Geologists, 111(1), 29-55.
1014 Song, X.Y., Wang, K.Y., Barnes, S.J., Yi, J.-N., and Schoneveld, L.E. (2020) Petrogenetic insights of
1015 chromite in ultramafic cumulates: Implications from the Xiarihamu intrusion, northern Tibet
1016 Plateau, China. American Mineralogist, 105, 479-497.
1017 Spaggiari, C.V., Kirkland, C.L., Smithies, R.H., Wingate, M.T.D., and Belousova, E. (2015)
1018 Transformation of an Archean craton margin during Proterozoic basin formation and
1019 magmatism: the Albany–Fraser Orogen, Western Australia. Precambrian Research, 266, 440-
1020 466.

Su, B.-X., Qin, K.-Z., Sakyi, P.A., Li, X.-H., Yang, Y.-H., Sun, H., Tang, D.-M., Liu, P.-P., Xiao, Q.-H., and Malaviarachchi, S.P.K. (2011) U–Pb ages and Hf–O isotopes of zircons from Late Paleozoic mafic–ultramafic units in the southern Central Asian Orogenic Belt: Tectonic implications and evidence for an Early-Permian mantle plume. Gondwana Research, 20(2-3), 516-531.

Taranovic, V., Barnes, S.J., Beresford, S.W., Williams, M.J., MacRae, C., and Schoneveld, L.E. (2021) Nova – Bollinger Ni – Cu Sulfide Ore Deposits, Fraser Zone, Western Australia: Petrogenesis of the Host Intrusions. Economic Geology, in press.

Thakurta, J., Ripley, E.M., and Li, C. (2014) Platinum group element geochemistry of sulfide-rich horizons in the Ural-Alaskan-type ultramafic complex of Duke Island, southeastern Alaska. Economic Geology and the Bulletin of the Society of Economic Geologists, 109(3), 643-659.

Thakurta, J., Ripley, E.M., and Li, C.S. (2008) Pre-requisites for Sulphide-poor PGE and Sulphide-rich Cu-Ni-PGE Mineralization in Alaskan-type Complexes. Journal of the Geological Society of India, 72(5), 611-622.

Wei, B., Wang, C.Y., Li, C., and Sun, Y. (2013) Origin of PGE-Depleted Ni-Cu Sulfide Mineralization in the Triassic Hongqiling No. 7 Orthopyroxenite Intrusion, Central Asian Orogenic Belt, Northeastern China. Economic Geology, 108(8), 1813-1831.

Workman, R.K., and Hart, S.R. (2005) Major and trace element composition of the depleted MORB mantle (DMM). Earth and Planetary Science Letters, 231(1-2), 53-72.

Xue, S., Qin, K., Li, C., Tang, D., Mao, Y.-J., and Qi L. (2016) Geochronological, Petrological, and Geochemical Constraints on Ni-Cu Sulfide Mineralization in the Poyi Ultramafic-Troctolitic Intrusion in the Northeast Rim of the Tarim Craton, Western China. Economic Geology, 111, 1465-1484.

Yang, S.-H., Maier, W.D., Hanski, E.J., Lappalainen, M., Santaguida, F., and Maatta, S. (2013) Origin of ultra-nickeliferous olivine in the Kevitsa Ni-Cu-PGE-mineralized intrusion, northern Finland. Contributions to Mineralogy and Petrology, 166(1), 81-95.

Yao, Z.-s., and Mungall, J.E. (2021) Linking the Siberian Flood Basalts and Giant Ni-Cu-PGE Sulfide Deposits at Norilsk. Journal of Geophysical Research: Solid Earth, 126(3), e2020JB020823.

Yao, Z., Qin, K.Z., and Mungall, E. (2018) Tectonic controls on Ni and Cu contents of primary mantle-derived magmas for the formation of magmatic sulfide deposits. American Mineralogist, online AM-18-106392.

Zhang, M., Li, C., Fu, P., Hu, P., and Ripley, E. (2011) The Permian Huangshanxi Cu–Ni deposit in western China: intrusive–extrusive association, ore genesis, and exploration implications. Mineralium Deposita, 46(2), 153-170.

Zhang, Z.C., Ma, J.W., Wang, F.S., Hao, Y.L., and Mahoney, J.J. (2005) Mantle Plume Activity and Melting Conditions: Evidence From Olivines in Picritic-Komatiitic Rocks From the Emeishan Large Igneous Province, Southwestern China. Episodes, 28(3), 171-176.

Zhang, Z.C., Mao, J.W., Chai, F.M., Yan, S.H., Chen, B.L., and Pirajno, F. (2009) Geochemistry of the Permian Kalatongke Mafic Intrusions, Northern Xinjiang, Northwest China: Implications for the Genesis of Magmatic Ni-Cu Sulfide Deposits. Economic Geology, 104(2), 185-203.

Figure captions

Figure 1 Sobolev et al. (2008) and GEOROC basaltic olivine data set. A, Sobolev data, for continental and oceanic LIPs (CLIP, OLIP) and MORB. B, Sobolev CLIP data, excluding the outlying Gudchichinsky Picrites (Siberia) with 90th and 50th percentile data density contours. C Density shaded data cloud for Oceanic LIPs only (individual points are 95th percentile outliers) shown over the CLIP contours and with 90th percentile data contour on MORB olivines. D, Comparison of convergent margin data: data points are olivines from GEOROC data compilation for tholeiitic and picritic volcanic/subvolcanic rocks from continental (pink) and oceanic (green) convergent margin settings including active arcs, compared with Sobolev CLIP data density fields (grey).

Figure 2. Comparison of olivine from unmineralized intrusions, small intrusions and large LMIs combined, between LIP settings (A – 550 data points) and orogenic belt settings (B – 844 data points), both showing data points and contoured data density. A shows data points for LIP intrusions over outline for CLIP basalts from Sobolev et al. (Figure 1), B shows orogenic belt intrusions over 50th and 90th density contours for barren LIP intrusions. Field labelled MSFM is for olivines formed as fractional crystallization products of modelled sulfide-free mantle melts, based on computational modelling described in detail below.

Figure 3. Proterozoic plus Phanerozoic CLIP-LMI settings. A, Data points for mineralized intrusions over cloud for barren intrusions from Figure 2A. B, same dataset, mineralized only, subdivided by locality. Note that scale is trimmed to exclude extreme Ni enriched olivines from Kevitsa discussed below. In this and most following plots, red symbols indicate Mineralized, green indicated Disseminated or minor mineralization – see Methods section for definitions. Curve labelled MSFM is modelled outline for olivines derived from variably fractionated model sulfide free mantle melts (MSFM). Grey fields are data cloud for unmineralized LIP-related intrusions.

Figure 4. Orogenic belt settings – Proterozoic (A) + Phanerozoic (B). Data points for mineralized intrusions over cloud (yellow) for barren orogenic belt intrusions from Figure 2B and modelled outline for olivines derived from variably fractionated model sulfide free mantle melts (MSFM). CAOB = Central Asia Orogenic Belt in China; ACO = Appalachian-Caledonian Orogen; KBF = Kotalahti Belt (Svecofennian Orogen), Finland.

Figure 5. Ni-Fo plot for samples from the Kabanga–Musongati–Kapalagulu Belt. Contours on data densities for barren intrusions from CLIP and LMI grouping.

Figure 6. A) Olivines from the Sally Malay suite of intrusions in the Halls Creek Orogen, over data cloud for barren intrusions from orogenic belts (yellow). Savannah, Savannah North and Copernicus

host the known economic deposits, Dave Hill and Wilsons contain sparse localized disseminated sulfides. MSFM is theoretical range for olivines from sulfide-free mantle melts. B) Same data set, coloured by sulfide content of individual samples – B= barren (no visible sulfide, and/or less than 0.1% S), D=containing disseminated sulfide.

Figure 7. A, Olivines from small intrusions in the Central Asian Orogenic Belt in NW China and the Xiarihamu intrusion, Tibet. All intrusions are mineralized to varying degrees. Field for data from barren intrusions from orogenic belts (Figure 2). MSFM is model field for sulfide-free olivines from mantle melts. Note that: "Beishan" here represents a summary of the olivine data from the mafic-ultramafic intrusions located in the Beishan area, except the Poyi intrusion; the olivine data of Honqiling and Tulaergen deposits is collected from the disseminated mineralization. B, Same data set excluding Xiarihamu, subdivided by sulfide content of sample (B = <100 ppm Cu, D = >100 ppm Cu).

Figure 8. Ni vs Fo plot of olivines from intrusions in the Svecofennian (Kotalahti) Belt of central Finland. Contours are on data from barren intrusions in orogenic settings. MSFM is model field for sulfide-free olivines from mantle melts.

Figure 9. Ural-Alaskan Type Complexes. MSFM is model field for sulfide-free olivines from mantle melts.

Figure 10. Olivine compositions from the Kevitsa intrusion. Ni-PGE = High Ni-PGE tenor orezone, Ni tenors up to 30%. A, all data, subdivided by ore type. Xenolith is a sample of an ultramafic xenolith within this zone. "Normal" includes disseminated ores with a wide range of Ni tenors. Most Ni depleted samples are from zones of "False Ore", pyrrhotite-rich disseminated sulfides associated with country rock metasediment xenoliths. Ni-PGE ores are defined on the basis of high Ni and PGE tenors in sulfide (Yang et al., 2013). B, Ni-PGE oretype only, data subdivided by sample for all samples with >6 individual spot analyses. Note the strong negative correlation between Ni and Fo content within samples. MSFM is model field for sulfide-free olivines from mantle melts.

Figure 11. Olivine compositions in the Nova-Bollinger system. A, Ni vs Fo plot, shapes indicate host intrusion, colours are arbitrary indications of range of Ni-Fo. Fields for barren orogenic belt intrusions (yellow) and 90th percentile outline for barren LIP intrusions (grey dashed lines). Arrows indicate locations of different composition types on (B), projected long section in vertical plane, looking north, through entire system. Note the most Ni-depleted Fo rich olivines are located within the upper part of the Upper Intrusion, more Fe rich with trends towards Ni enriched olivine are in the Lower (ore-bearing) intrusion.

Figure 12 – model curves for olivine compositions generated by low-pressure fractional crystallization from various starting magmas (see Appendix)

Figure 13 Low-pressure fractional crystallization (FC) trends for the indicated pressure, fO2 and magma water content. The proportion ratios of olivine and sulfide in each crystallization increment are assumed as 50, 100, 200 and 500. The partition coefficient of Ni between sulfide and melt is calculated by the recent comprehensive model from Kiseeva and Wood (2015). In (B), the mantle source in flux melting is assumed to enrich in Ni (~3050 ppm), because the slab-metasomatized mantle wedge can show extreme enrichment of Ni and fluid mobile elements (Savov et al., 2007).

Figure 14. Model single-stage batch equilibrium calculations for olivine and sulfide Ni contents as a function of silicate melt/sulfide melt mass ratio R factor for the four idealized silicate melt compositions indicated in Table 1. Sulfide equilibrates with mixture of 95% silicate melt, 5% olivine. See Barnes et al. (2013) for details of calculation procedure.

Figure 15. Cartoon of olivine-trapped liquid reaction. A. Flowing slurry of silicate + sulfide melts and olivine. B, accumulation of olivine, sulfide in different proportions to form a cumulate mush with ~40% silicate melt. Phases assumed to have the same compositions as A. C, cooling and equilibrium crystallization of the trapped intercumulus liquid causes olivine to evolve towards more Fe rich composition, hence also becoming more Ni rich due the Fe-Ni exchange reaction (equns. 1,2).

Figure 16. Calculation showing theoretical effect of trapped liquid equilibration in olivine-sulfide orthocumulates (olivine-plagioclase orthocumulate in the basaltic case) with 5% modal % sulfide, for various silicate liquid compositions. Dash lines join points for the same R factor. “Original” compositions, corresponding to stage A in Figure 15, are olivines in equilibrium with sulfide and silicate liquid (95% liquid, 5% olivine) for different values of R and different starting silicate melt compositions (Table 1) corresponding to komatiite with 30% MgO, plume “picrite” basalt with 18% MgO , Ferropicrite with 14% MgO and MORB basalt (8% MgO), all being representative compositions from the modelling results described above. Note that a larger shift in olivine Fo is assumed for the cumulate from the low-Mg mafic magma owing to a lower modal proportion of olivine in the cumulus assemblage – see Barnes (1986).

Figure 17. Model for generation of Ni-enriched olivine by “cannibalization” of previously formed sulfide. A, initial formation of Ni-rich sulfide liquid pool from an Mg-rich magma. B, flushing of flow pathway by more evolved magma carrying relatively low-Fo, Fe-enriched olivine. Reaction of this olivine with stage-A Ni-rich sulfide causes Ni content of olivine to increase due to the Fe-Ni exchange reaction (equation 1).

Figure 18. Schematic diagram showing the multiple factors influencing final olivine compositions. Single dashed lines indicate olivine-only fractional crystallization (FX) from idealized primitive mantle melts from deep plume source and from flux melting of hydrated mantle. FX(ol-sul) indicates effect of fractional crystallization/liquation of a cotectic olivine-sulfide assemblage from primitive plume melt. TL = effect of re-equilibration during solidification of trapped intercumulus liquid, with and without presence of cumulus sulfide. Recharge and mixing indicates effect of mixing fractionated and primitive magmas (Gleeson & Gibson, 2019). Batch sulfide extraction indicates effect of addition of xenomelt sulfide and batch equilibration with melt and olivine (Figure 14).

Appendix Figure A1. The influences of crystallization environments (A. crystallization pressure; B. initial H2O content; and C-D. oxygen fugacity) on the Ni contents of olivine grains that are crystallized from parental magma derived by the adiabatic decompression melting in plume (A-C) and the flux melting of DMM in subduction zone (D).

Table 1.

Starting compositions for batch equilibrium - trapped liquid reaction model in Figure 16. (eqm) indicates composition of olivine or sulfide liquid at R>10,000

	Kom	Plume bas 18	Ferropicrite 14	MORB 8
Ni sil	1600	660	350	100
FeOsil	10.0	12	14.0	8.5
MgOsil	30.0	18.0	14.0	8.0
Cu sil	50	100	100	200
NiOl (eqm)	3191	3430	2444	1505
FoOl (eqm)	93.8	88.8	84.4	85.4
Sul liq (eqm)	37.9	24.9	13.6	6.9
T	1600	1380	1280	1140

fig 1

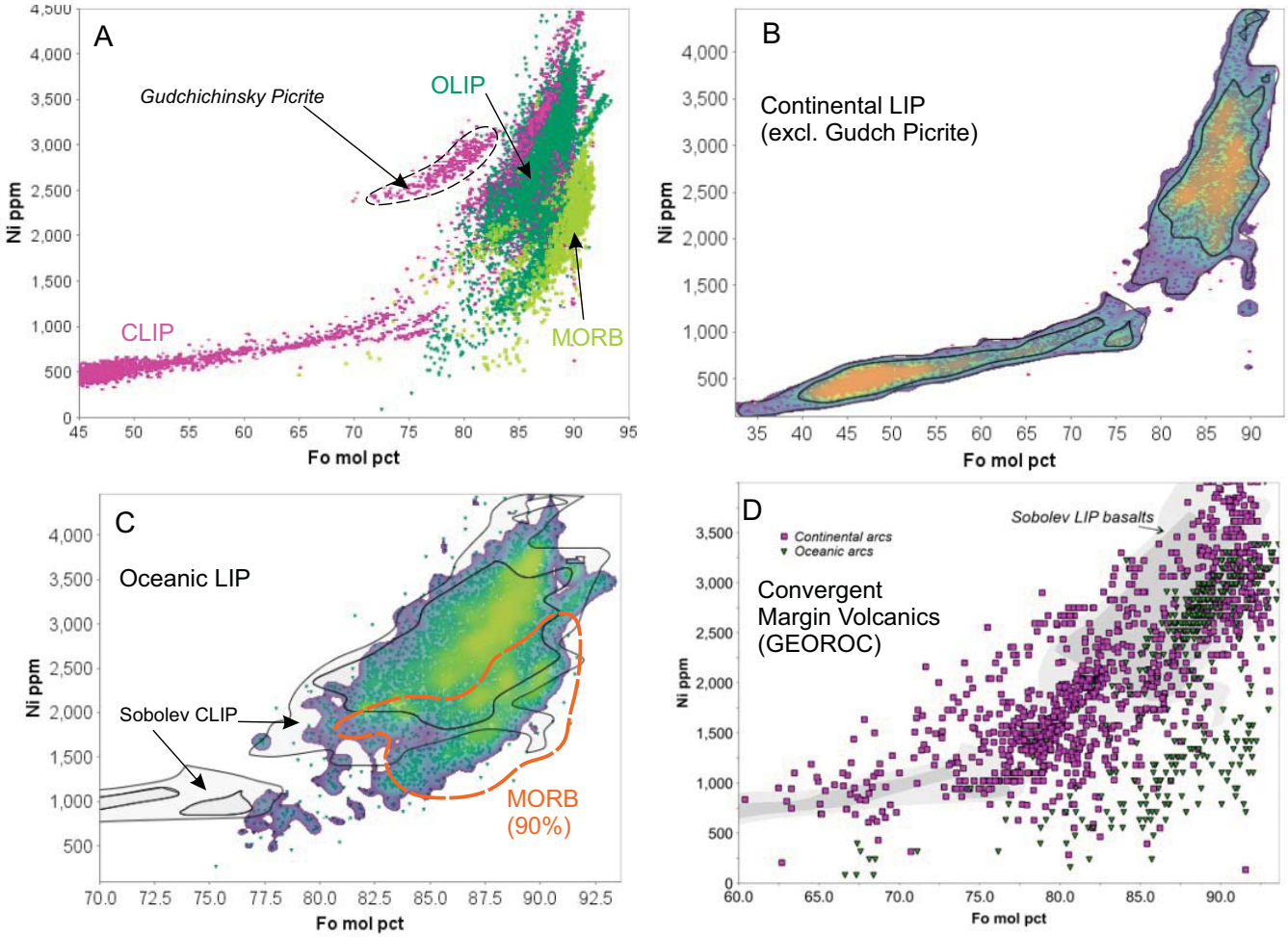
A
Gudchichinsky Picrite
OLIP
CLIP
MORB
Ni ppm
Fo mol pct
B
Continental LIP
(excl. Gudch Picrite)
Ni ppm
Fo mol pct
C
Oceanic LIP
Sobolev CLIP
MORB
(90%)
Ni ppm
Fo mol pct
D
Continental arcs
Oceanic arcs
Sobolev LIP basalts
Convergent
Margin Volcanics
(GEOROC)
Ni ppm
Fo mol pct

fig 2

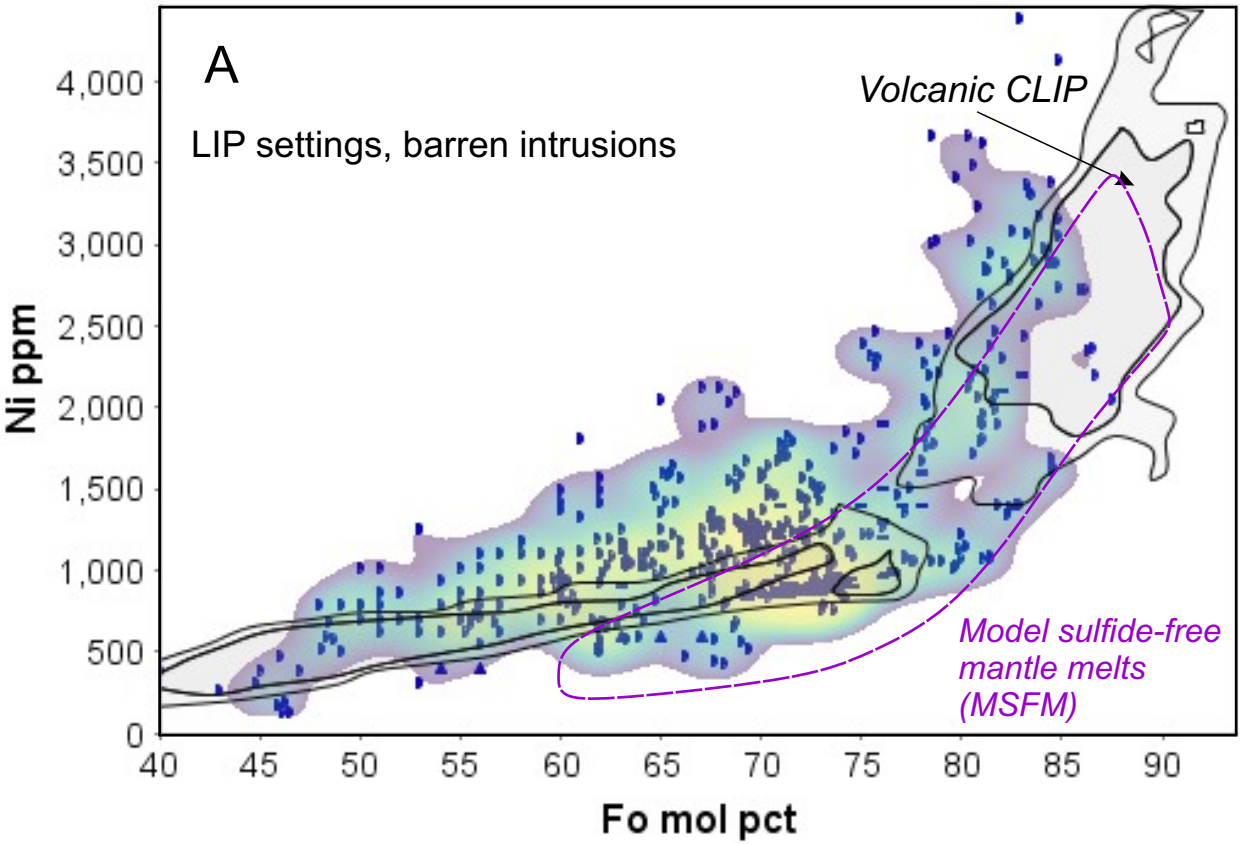
A
LIP settings, barren intrusions
Volcanic CLIP
Model sulfide-free mantle melts (MSFM)
Ni ppm
Fo mol pct
0
500
1,000
1,500
2,000
2,500
3,000
3,500
4,000
40
45
50
55
60
65
70
75
80
85
90

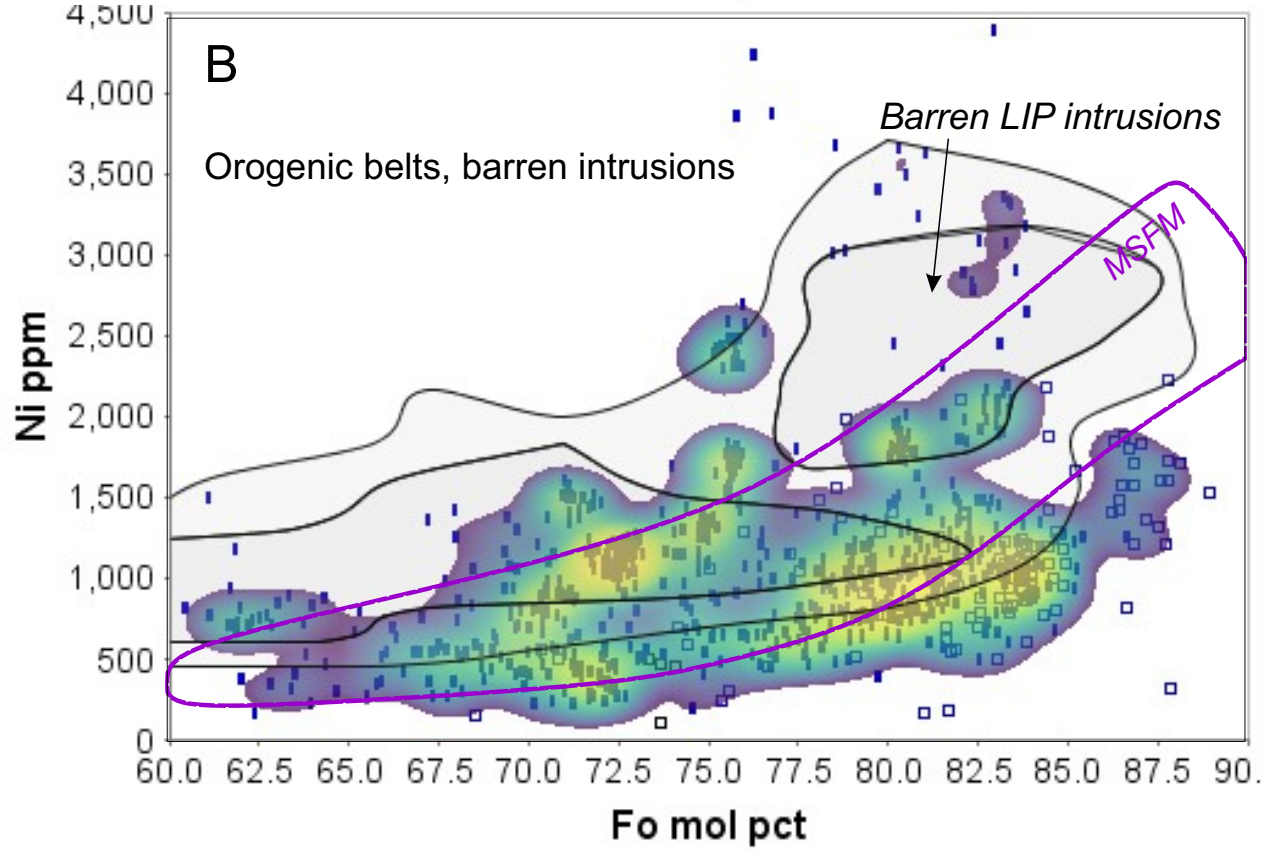
B
Orogenic belts, barren intrusions
Barren LIP intrusions
MSFM
Ni ppm
Fo mol pct
0
500
1,000
1,500
2,000
2,500
3,000
3,500
4,000
4,500
60.0
62.5
65.0
67.5
70.0
72.5
75.0
77.5
80.0
82.5
85.0
87.5
90.

fig 3

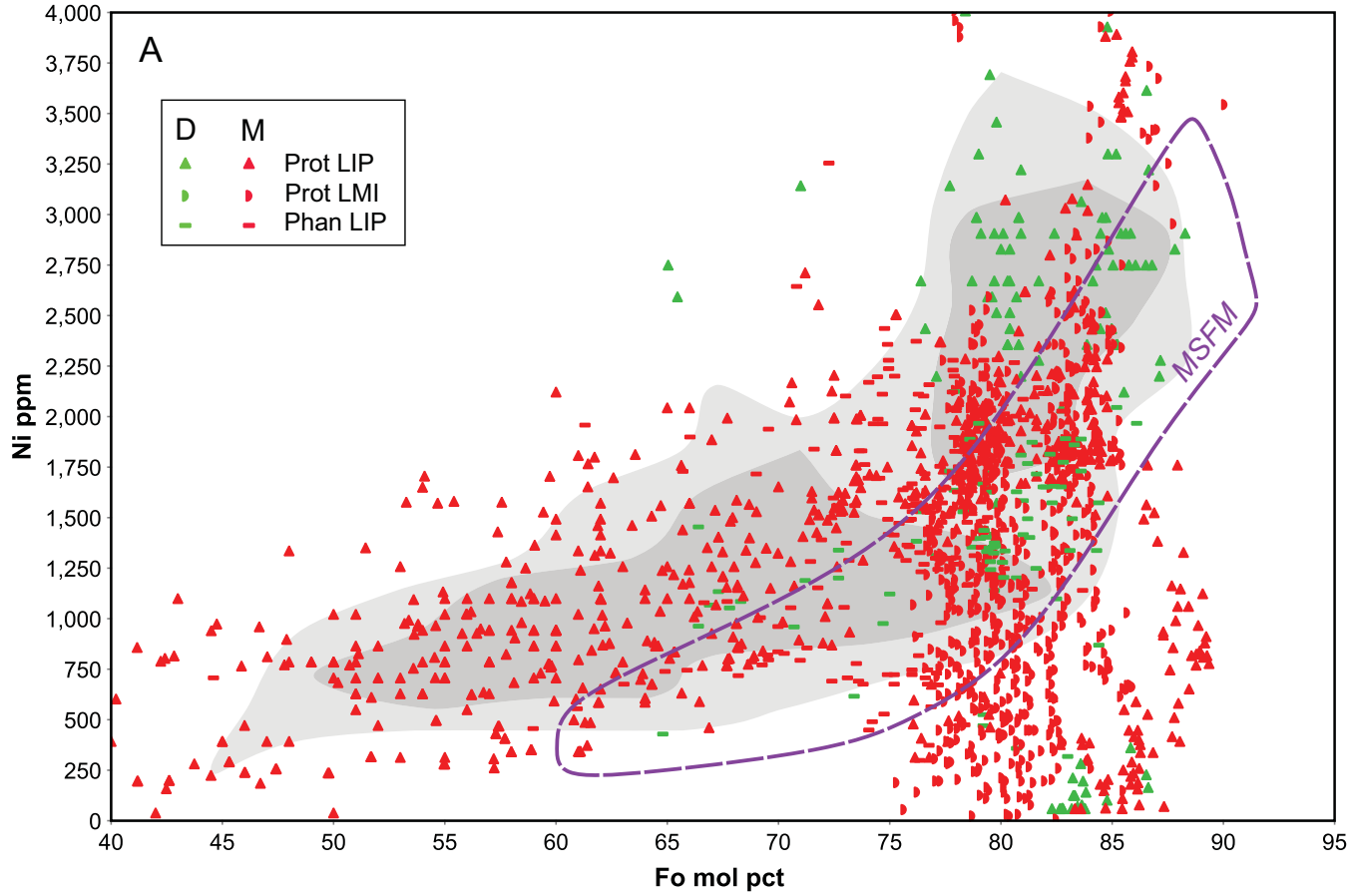
A
D M
Prot LIP
Prot LMI
Phan LIP
MSFM
Ni ppm
Fo mol pct
4,000
3,750
3,500
3,250
3,000
2,750
2,500
2,250
2,000
1,750
1,500
1,250
1,000
750
500
250
0
40
45
50
55
60
65
70
75
80
85
90
95

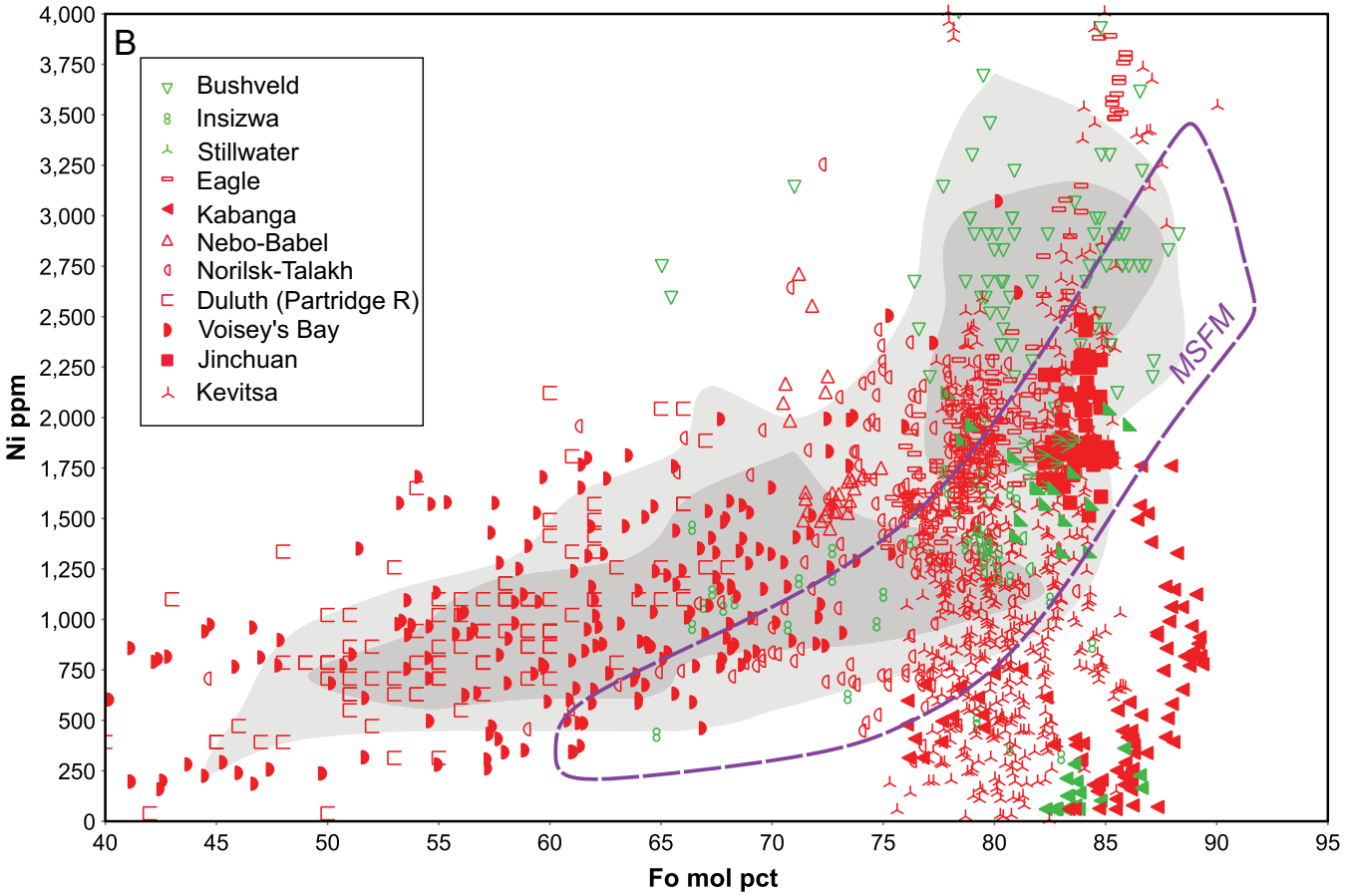
B
Bushveld
Insizwa
Stillwater
Eagle
Kabanga
Nebo-Babel
Norilsk-Talakh
Duluth (Partridge R)
Voisey's Bay
Jinchuan
Kevitsa
MSFM
Ni ppm
Fo mol pct
4,000
3,750
3,500
3,250
3,000
2,750
2,500
2,250
2,000
1,750
1,500
1,250
1,000
750
500
250
0
40
45
50
55
60
65
70
75
80
85
90
95

fig 4

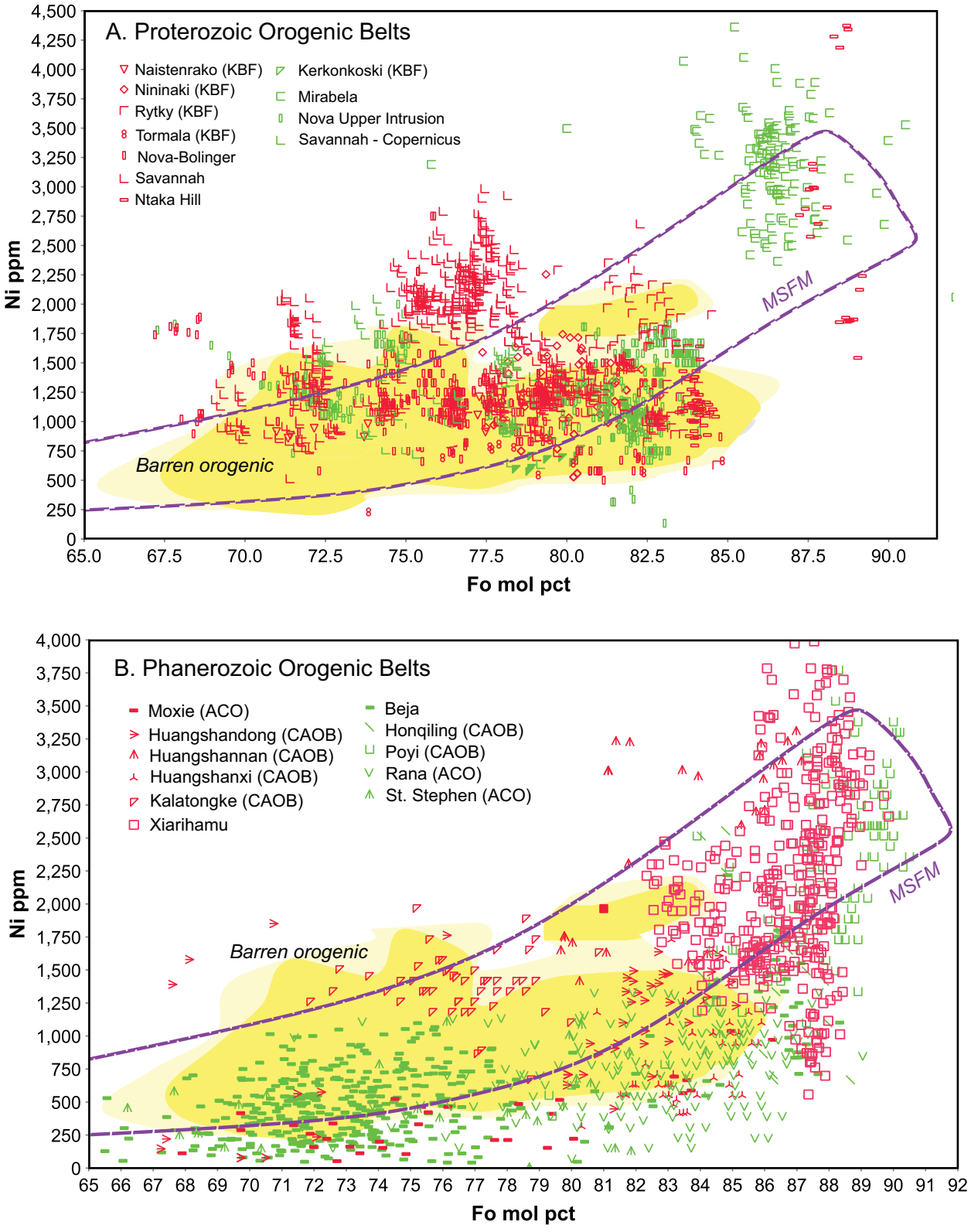
A. Proterozoic Orogenic Belts
Naistenrako (KBF)
Nininaki (KBF)
Rytky (KBF)
Tormala (KBF)
Nova-Bolinger
Savannah
Ntaka Hill
Kerkonkoski (KBF)
Mirabela
Nova Upper Intrusion
Savannah - Copernicus
Barren orogenic
MSFM
Ni ppm
Fo mol pct
B. Phanerozoic Orogenic Belts
Moxie (ACO)
Huangshandong (CAOB)
Huangshannan (CAOB)
Huangshanxi (CAOB)
Kalatongke (CAOB)
Xiarihamu
Beja
Honqiling (CAOB)
Poyi (CAOB)
Rana (ACO)
St. Stephen (ACO)
Barren orogenic
MSFM
Ni ppm
Fo mol pct

fig 5

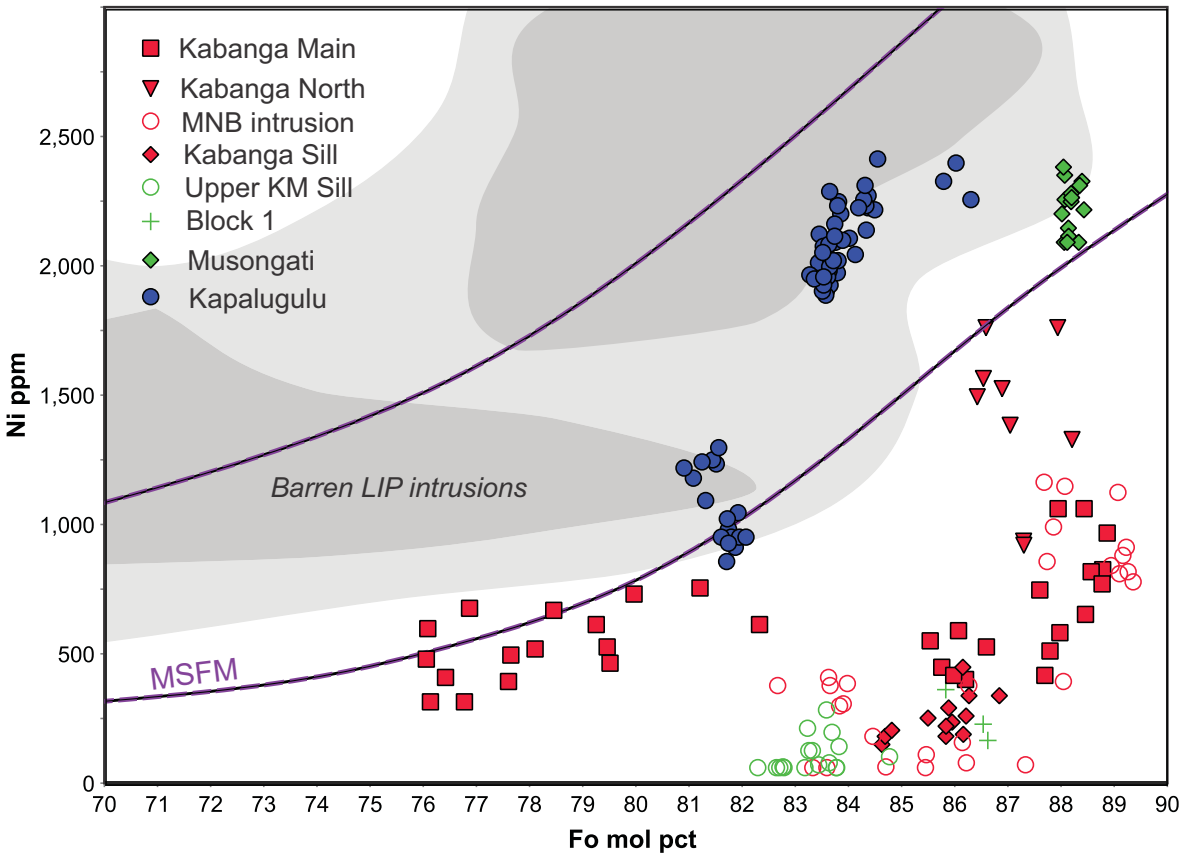
Kabanga Main
Kabanga North
MNB intrusion
Kabanga Sill
Upper KM Sill
Block 1
Musongati
Kapalugulu
Barren LIP intrusions
MSFM
Ni ppm
Fo mol pct
0
500
1,000
1,500
2,000
2,500
70
71
72
73
74
75
76
77
78
79
80
81
82
83
84
85
86
87
88
89
90

fig 6

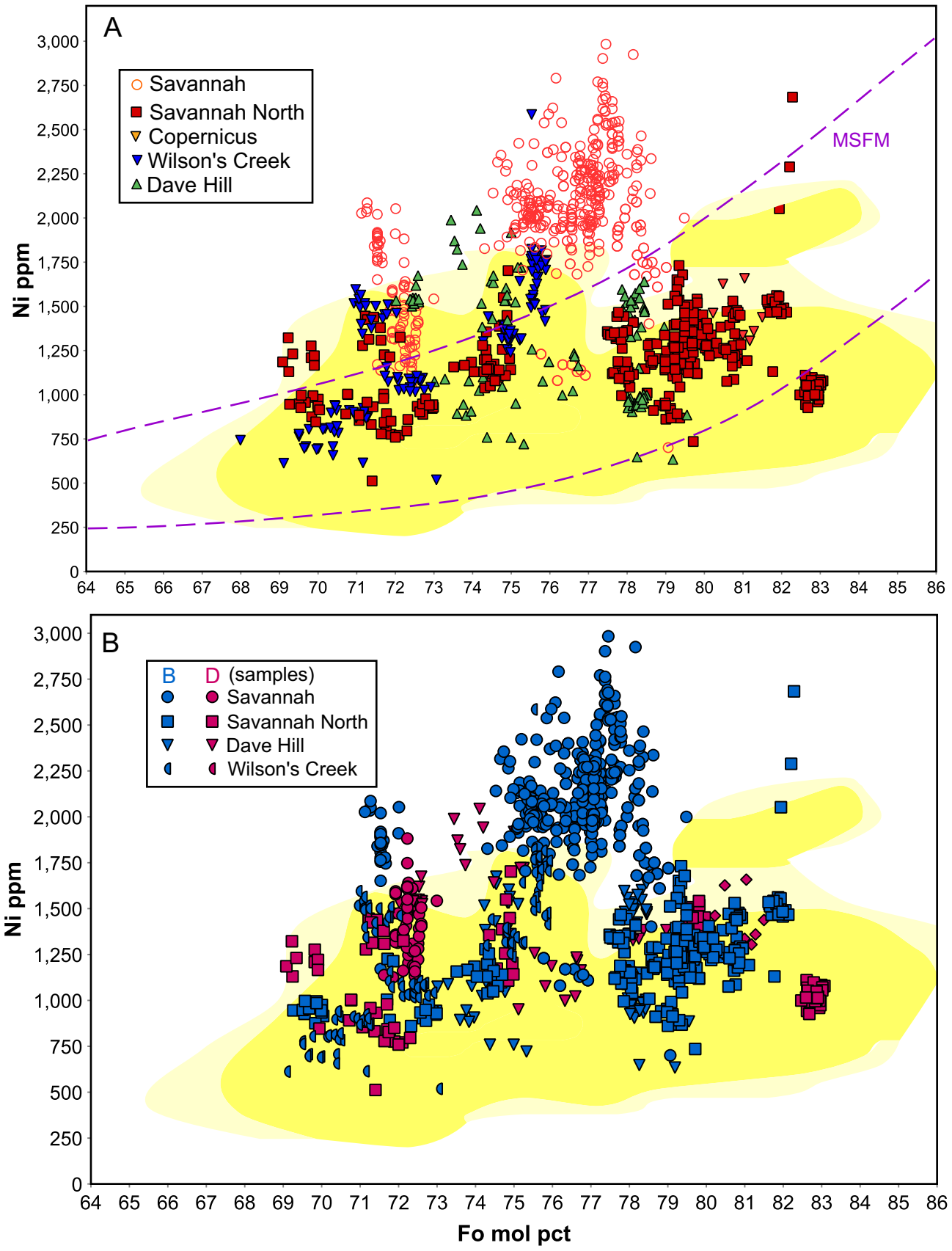
A
Savannah
Savannah North
Copernicus
Wilson's Creek
Dave Hill
MSFM
Ni ppm
3,000
2,750
2,500
2,250
2,000
1,750
1,500
1,250
1,000
750
500
250
0
64 65 66 67 68 69 70 71 72 73 74 75 76 77 78 79 80 81 82 83 84 85 86
B
B D (samples)
Savannah
Savannah North
Dave Hill
Wilson's Creek
Ni ppm
Fo mol pct

fig 7

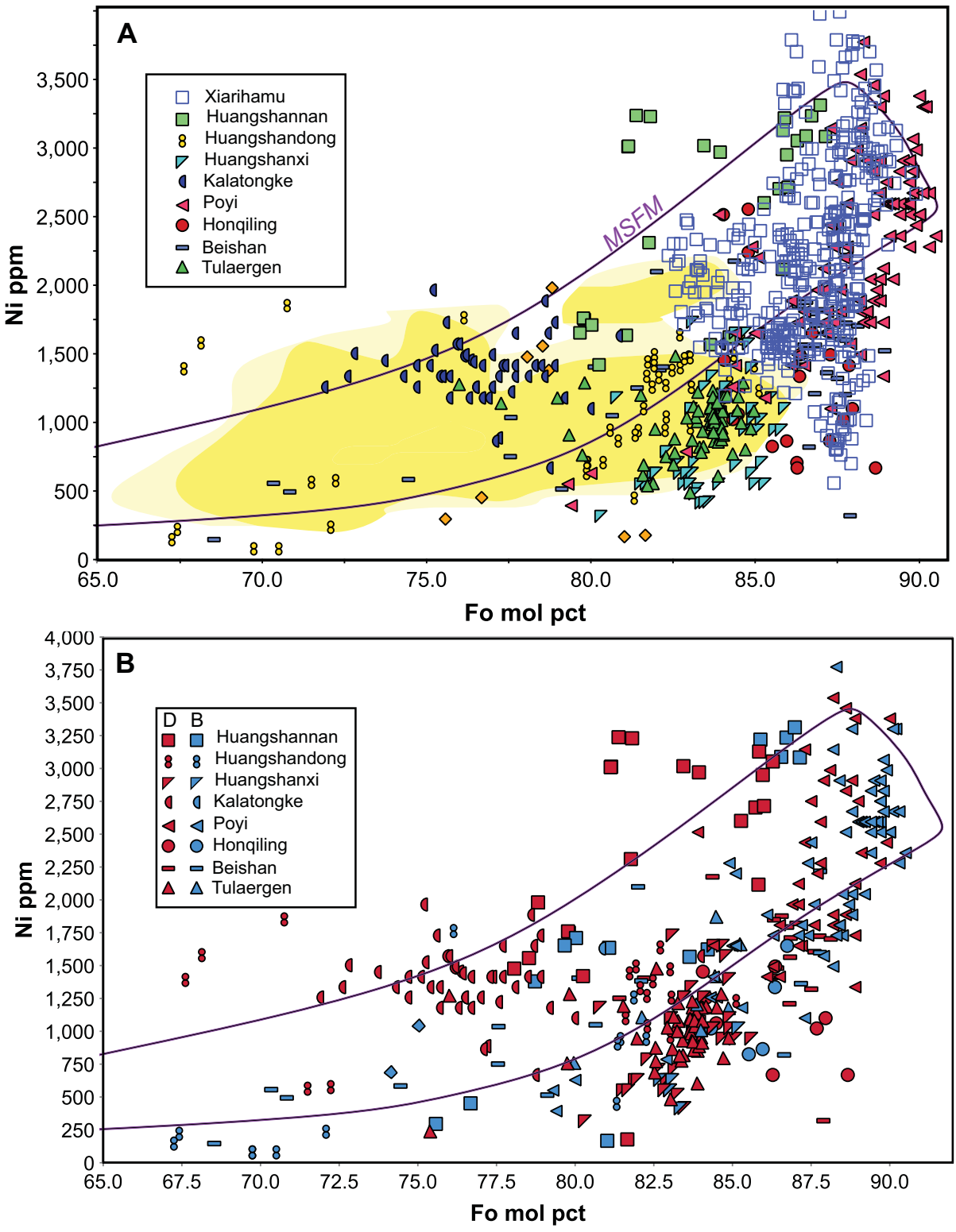
A
Xiarihamu
Huangshannan
Huangshandong
Huangshanxi
Kalatongke
Poyi
Honqiling
Beishan
Tulaergen
MSFM
Ni ppm
Fo mol pct
B
D B
Huangshannan
Huangshandong
Huangshanxi
Kalatongke
Poyi
Honqiling
Beishan
Tulaergen
Ni ppm
Fo mol pct

fig 8

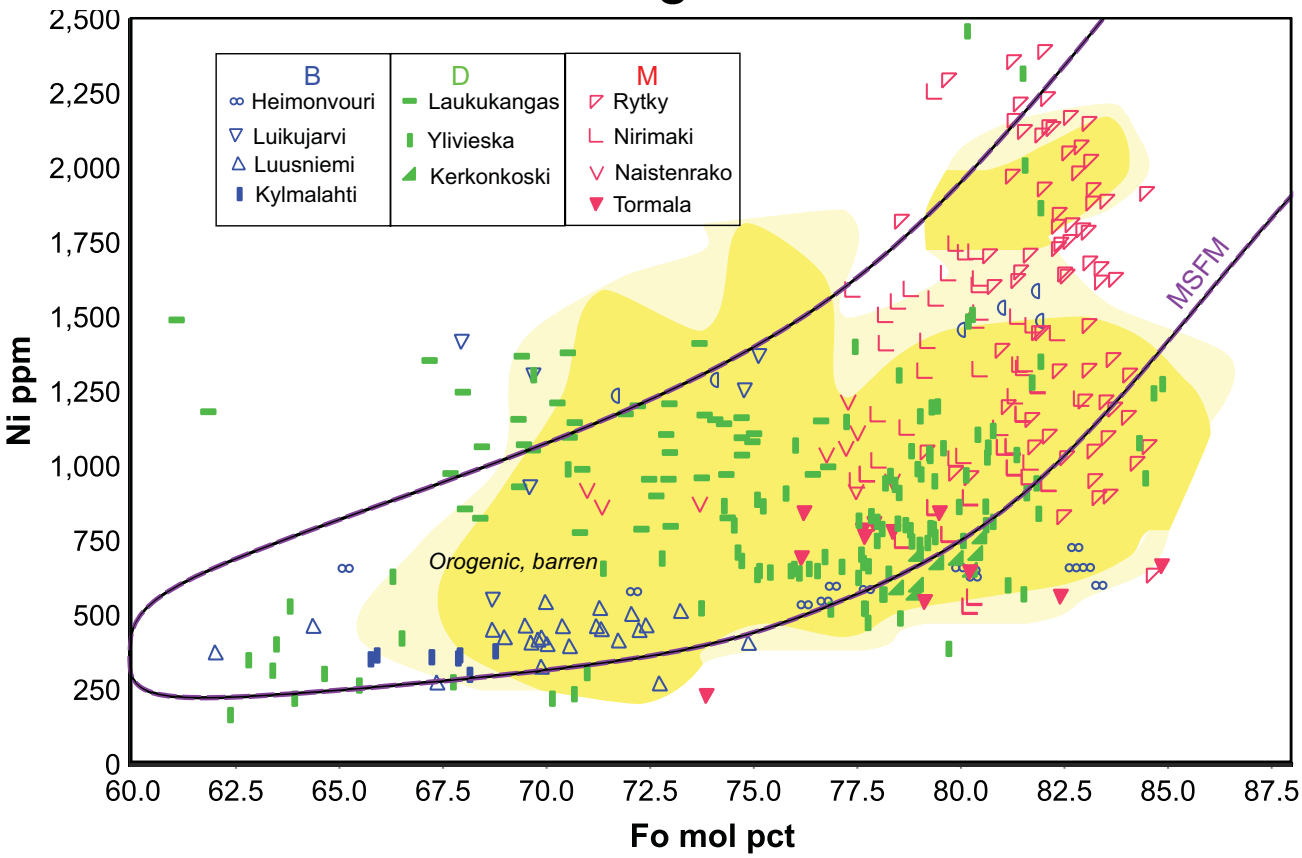
B
Heimonvouri
Luikujarvi
Luusniemi
Kylmalahti
D
Laukukangas
Ylivieska
Kerkonkoski
M
Rytky
Nirimaki
Naistenrako
Tormala
Orogenic, barren
MSFM
Ni ppm
Fo mol pct
2,500
2,250
2,000
1,750
1,500
1,250
1,000
750
500
250
0
60.0
62.5
65.0
67.5
70.0
72.5
75.0
77.5
80.0
82.5
85.0
87.5

fig 9

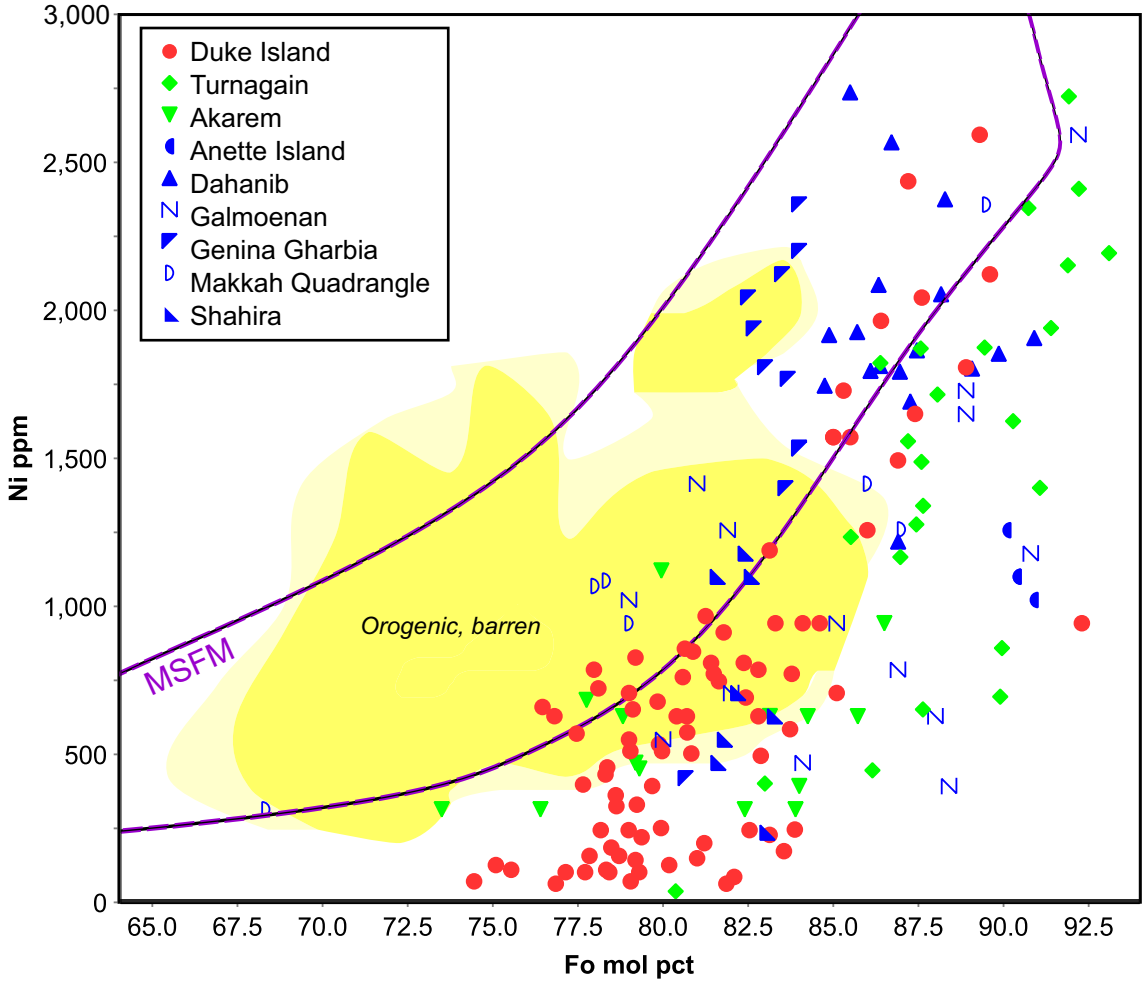
Duke Island
Turnagain
Akarem
Anette Island
Dahanib
Galmoenan
Genina Gharbia
Makkah Quadrangle
Shahira
Orogenic, barren
MSFM
Ni ppm
Fo mol pct
3,000
2,500
2,000
1,500
1,000
500
0
65.0
67.5
70.0
72.5
75.0
77.5
80.0
82.5
85.0
87.5
90.0
92.5

fig 10

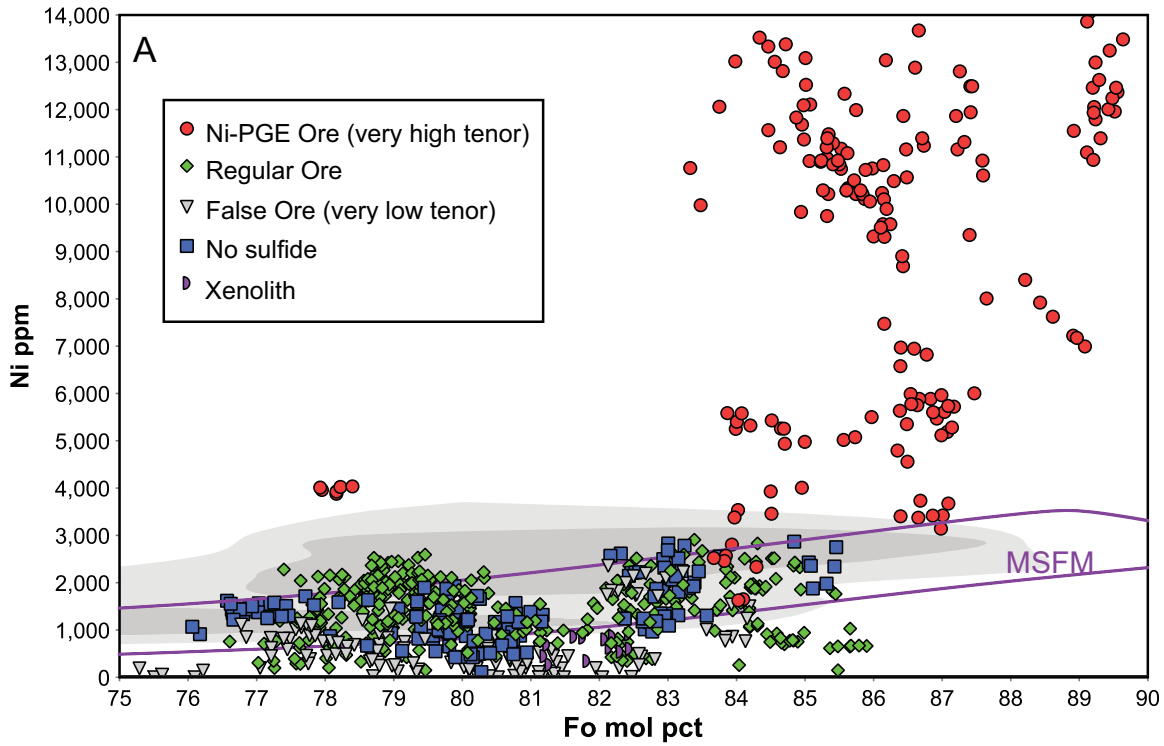
A
Ni-PGE Ore (very high tenor)
Regular Ore
False Ore (very low tenor)
No sulfide
Xenolith
MSFM
Ni ppm
Fo mol pct
14,000
13,000
12,000
11,000
10,000
9,000
8,000
7,000
6,000
5,000
4,000
3,000
2,000
1,000
0
75
76
77
78
79
80
81
82
83
84
85
86
87
88
89
90

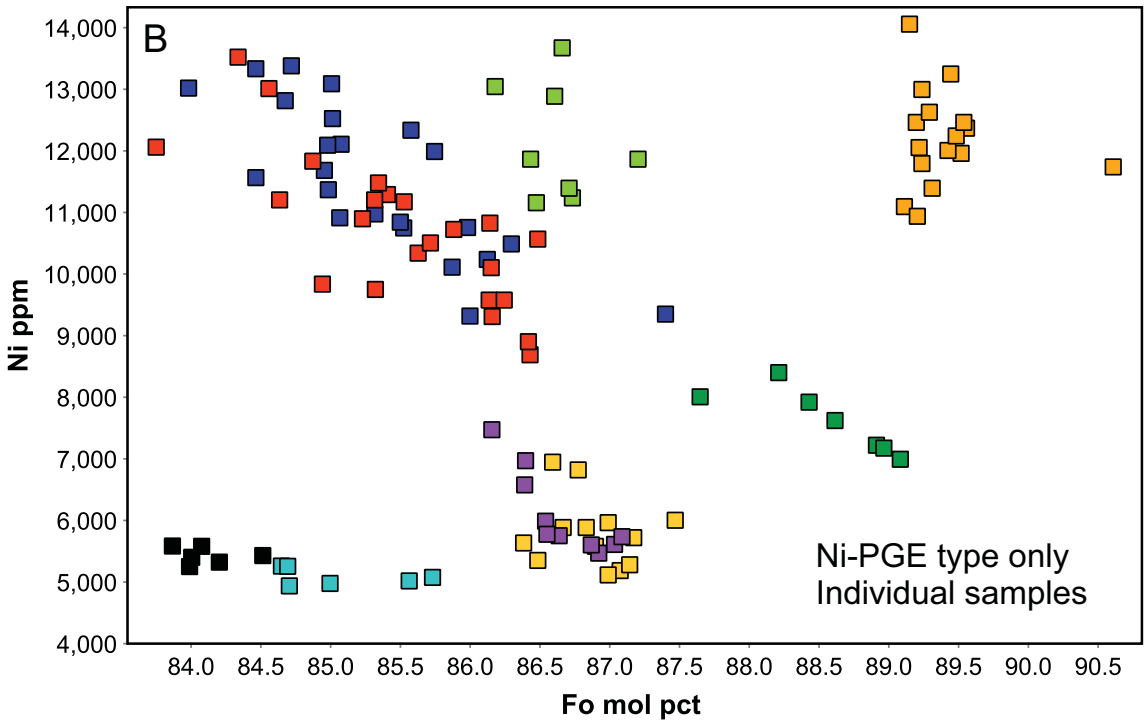
B
Ni-PGE type only
Individual samples
Ni ppm
Fo mol pct
14,000
13,000
12,000
11,000
10,000
9,000
8,000
7,000
6,000
5,000
4,000
84.0
84.5
85.0
85.5
86.0
86.5
87.0
87.5
88.0
88.5
89.0
89.5
90.0
90.5

fig 11

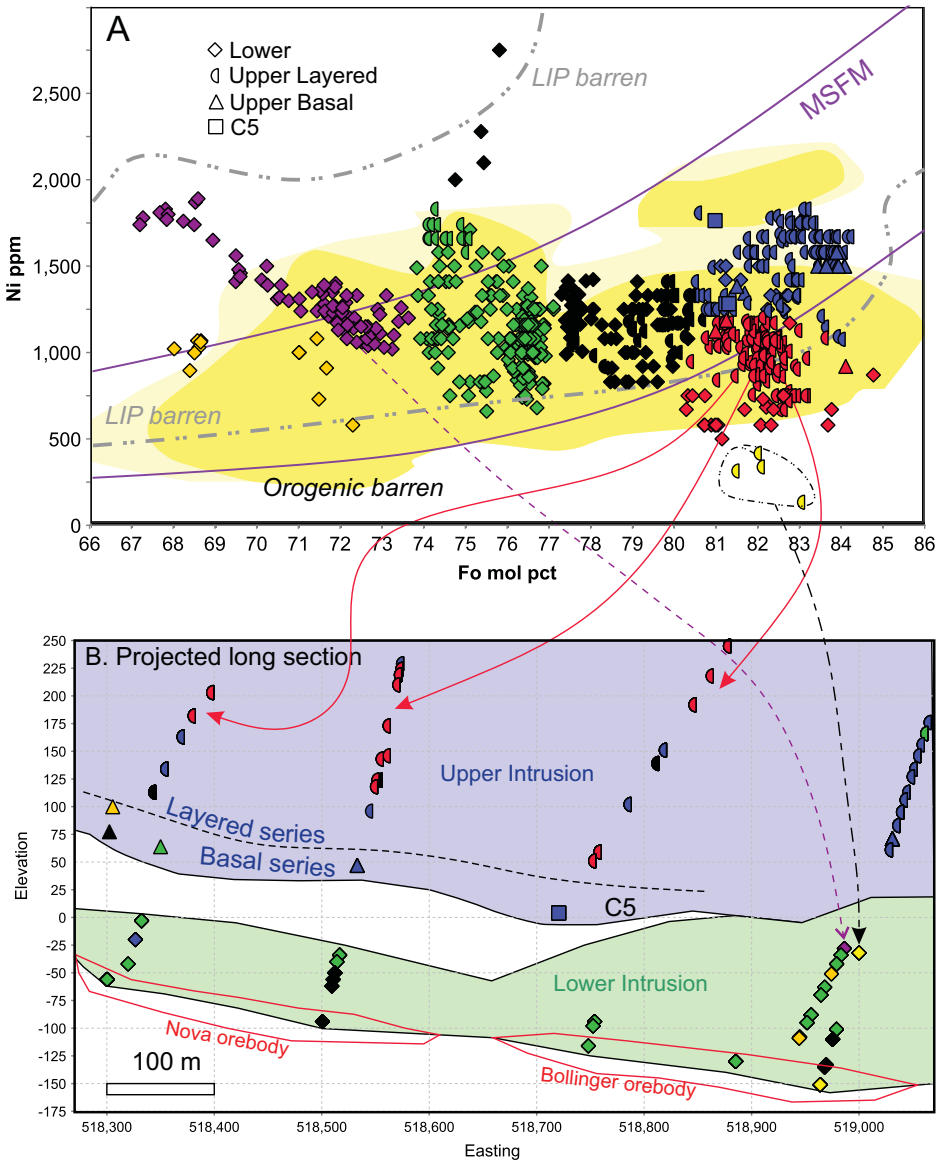
A
Lower
Upper Layered
Upper Basal
C5
LIP barren
MSFM
LIP barren
Orogenic barren
Ni ppm
Fo mol pct
B. Projected long section
Upper Intrusion
Layered series
Basal series
C5
Lower Intrusion
Nova orebody
Bollinger orebody
100 m
Elevation
Easting

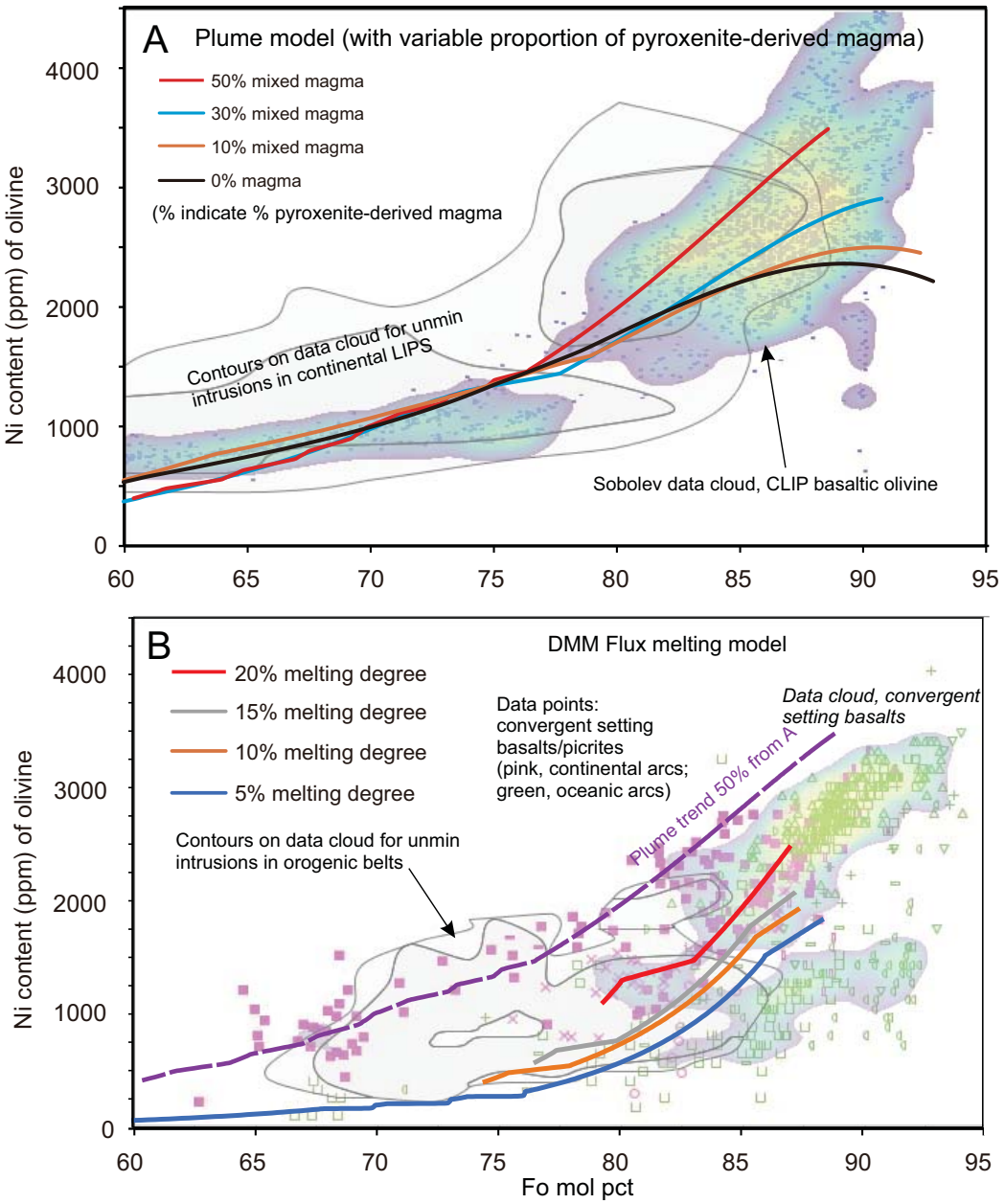
A
Plume model (with variable proportion of pyroxenite-derived magma)
50% mixed magma
30% mixed magma
10% mixed magma
0% magma
(% indicate % pyroxenite-derived magma
Contours on data cloud for unmin intrusions in continental LIPS
Sobolev data cloud, CLIP basaltic olivine
Ni content (ppm) of olivine
4000
3000
2000
1000
0
60
65
70
75
80
85
90
95
B
DMM Flux melting model
20% melting degree
15% melting degree
10% melting degree
5% melting degree
Data points:
convergent setting
basalts/picrites
(pink, continental arcs;
green, oceanic arcs)
Data cloud, convergent setting basalts
Plume trend 50% from A
Contours on data cloud for unmin intrusions in orogenic belts
Ni content (ppm) of olivine
Fo mol pct

fig 13

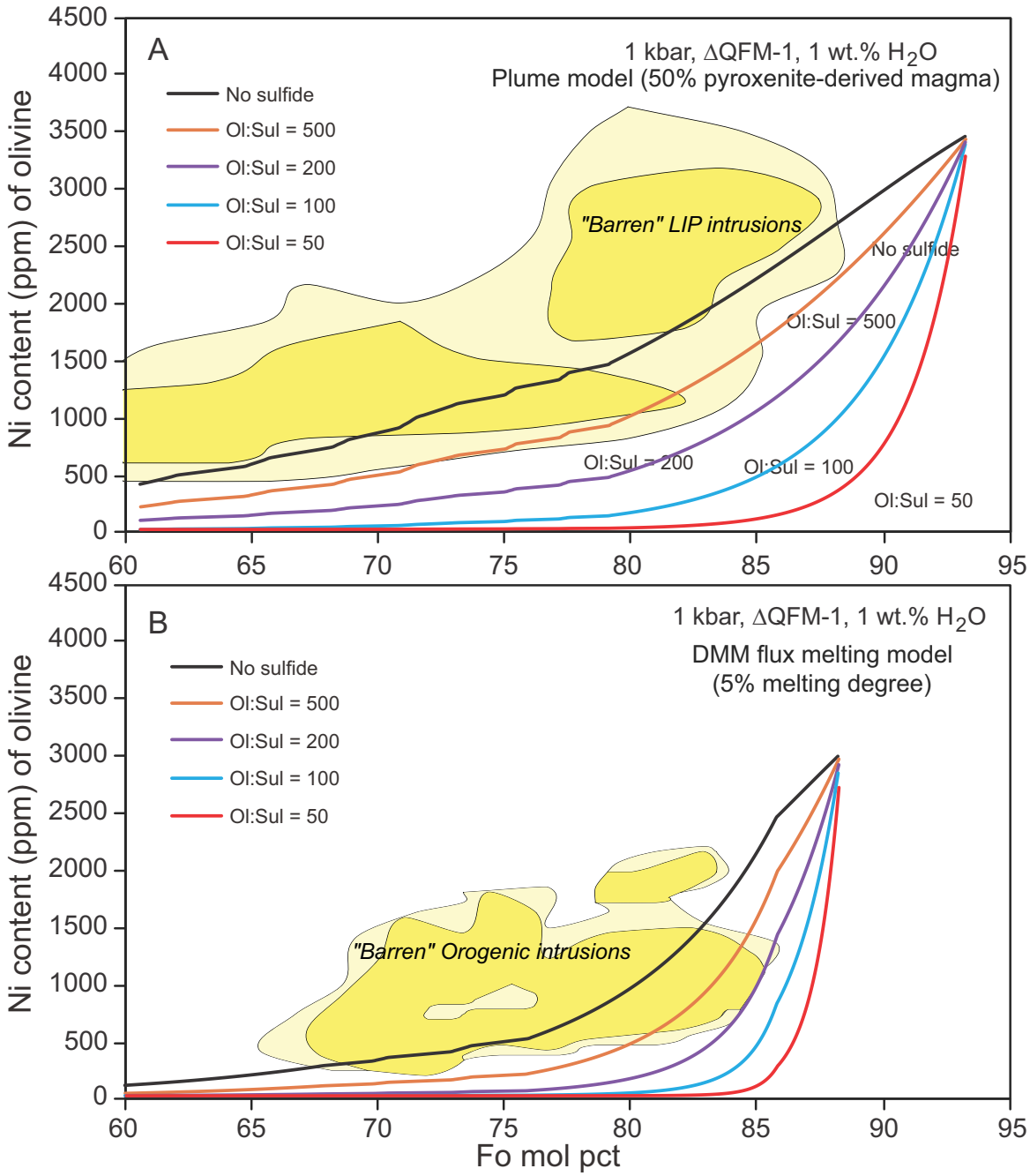
A
1 kbar, ΔQFM-1, 1 wt.% H2O
Plume model (50% pyroxenite-derived magma)
No sulfide
Ol:Sul = 500
Ol:Sul = 200
Ol:Sul = 100
Ol:Sul = 50
"Barren" LIP intrusions
No sulfide
Ol:Sul = 500
Ol:Sul = 200
Ol:Sul = 100
Ol:Sul = 50
Ni content (ppm) of olivine
B
1 kbar, ΔQFM-1, 1 wt.% H2O
DMM flux melting model
(5% melting degree)
No sulfide
Ol:Sul = 500
Ol:Sul = 200
Ol:Sul = 100
Ol:Sul = 50
"Barren" Orogenic intrusions
Ni content (ppm) of olivine
Fo mol pct

fig 14

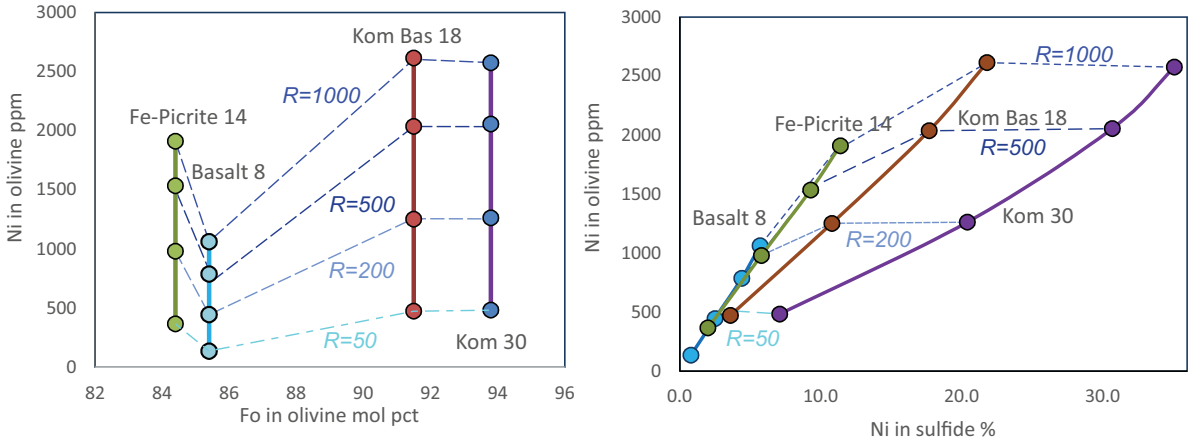
Ni in olivine ppm
Fo in olivine mol pct
Kom Bas 18
Fe-Picrite 14
Basalt 8
R=1000
R=500
R=200
R=50
Kom 30
Ni in sulfide %

fig 15

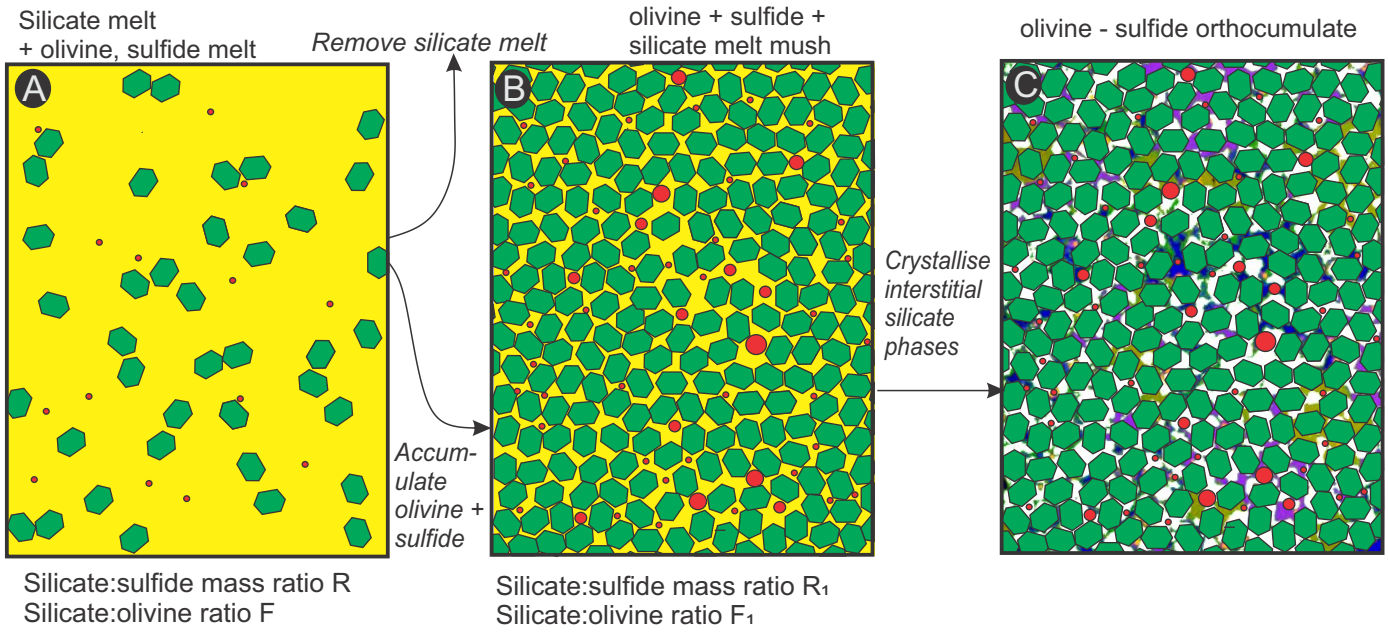
Silicate melt
+ olivine, sulfide melt
Remove silicate melt
olivine + sulfide +
silicate melt mush
olivine - sulfide orthocumulate
A
B
C
Accum-
ulate
olivine +
sulfide
Crystallise
interstitial
silicate
phases
Silicate:sulfide mass ratio R
Silicate:olivine ratio F
Silicate:sulfide mass ratio R1
Silicate:olivine ratio F1

fig 16

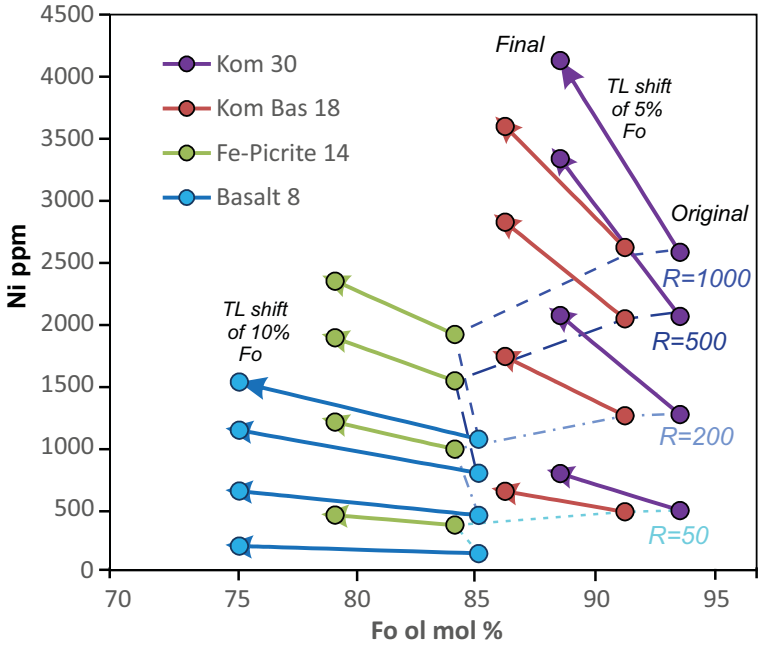
Kom 30
Kom Bas 18
Fe-Picrite 14
Basalt 8
Final
TL shift of 5% Fo
Original
R=1000
R=500
R=200
R=50
TL shift of 10% Fo
Ni ppm
Fo ol mol %
4500
4000
3500
3000
2500
2000
1500
1000
500
0
70
75
80
85
90
95

fig 17

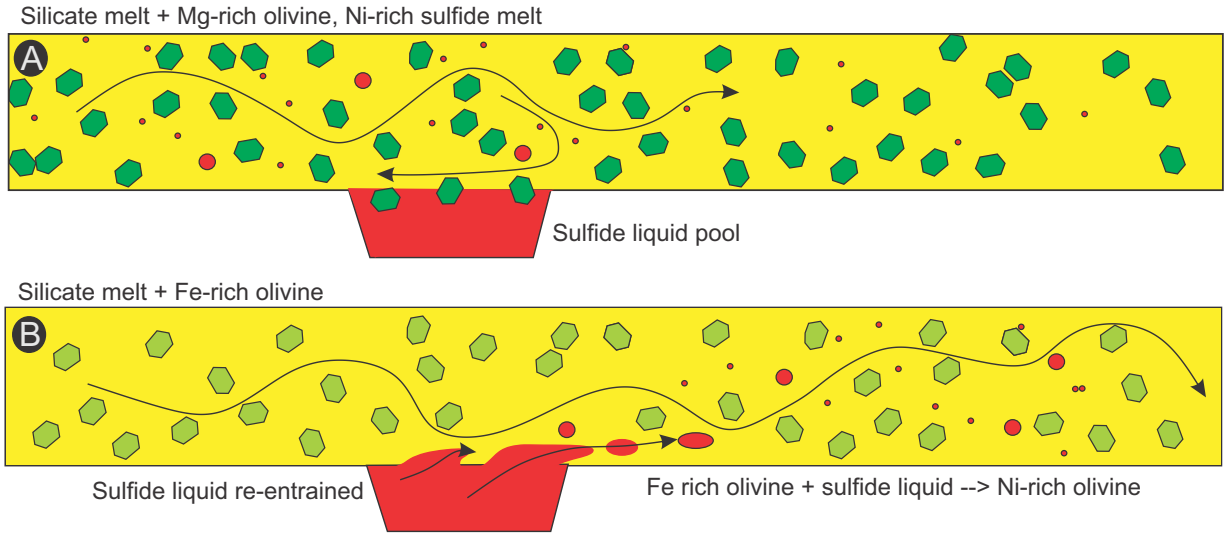
Silicate melt + Mg-rich olivine, Ni-rich sulfide melt
A
Sulfide liquid pool
Silicate melt + Fe-rich olivine
B
Sulfide liquid re-entrained
Fe rich olivine + sulfide liquid --> Ni-rich olivine

fig 18

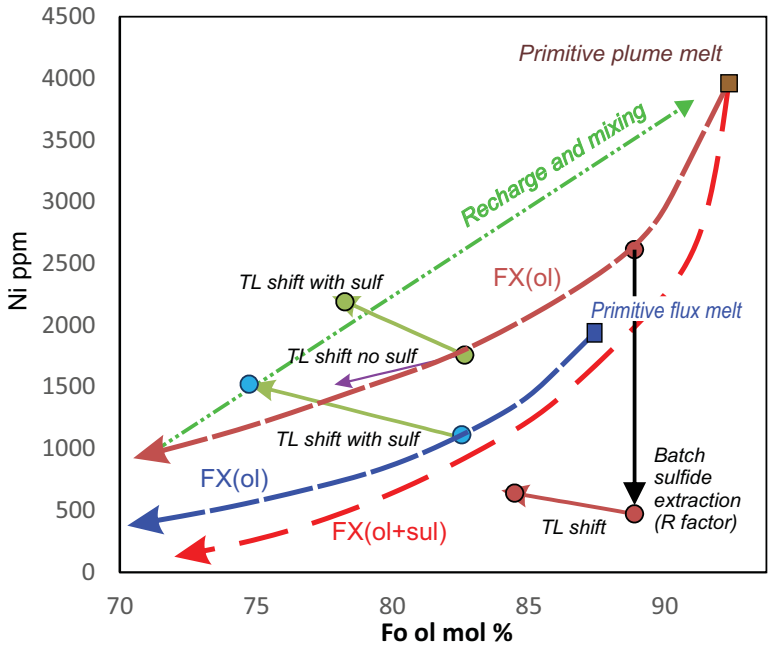
Primitive plume melt
Recharge and mixing
TL shift with sulf
FX(ol)
Primitive flux melt
TL shift no sulf
TL shift with sulf
FX(ol)
Batch
sulfide
extraction
(R factor)
TL shift
FX(ol+sul)
Ni ppm
4500
4000
3500
3000
2500
2000
1500
1000
500
0
70
75
80
85
90
Fo ol mol %

fig A1-1

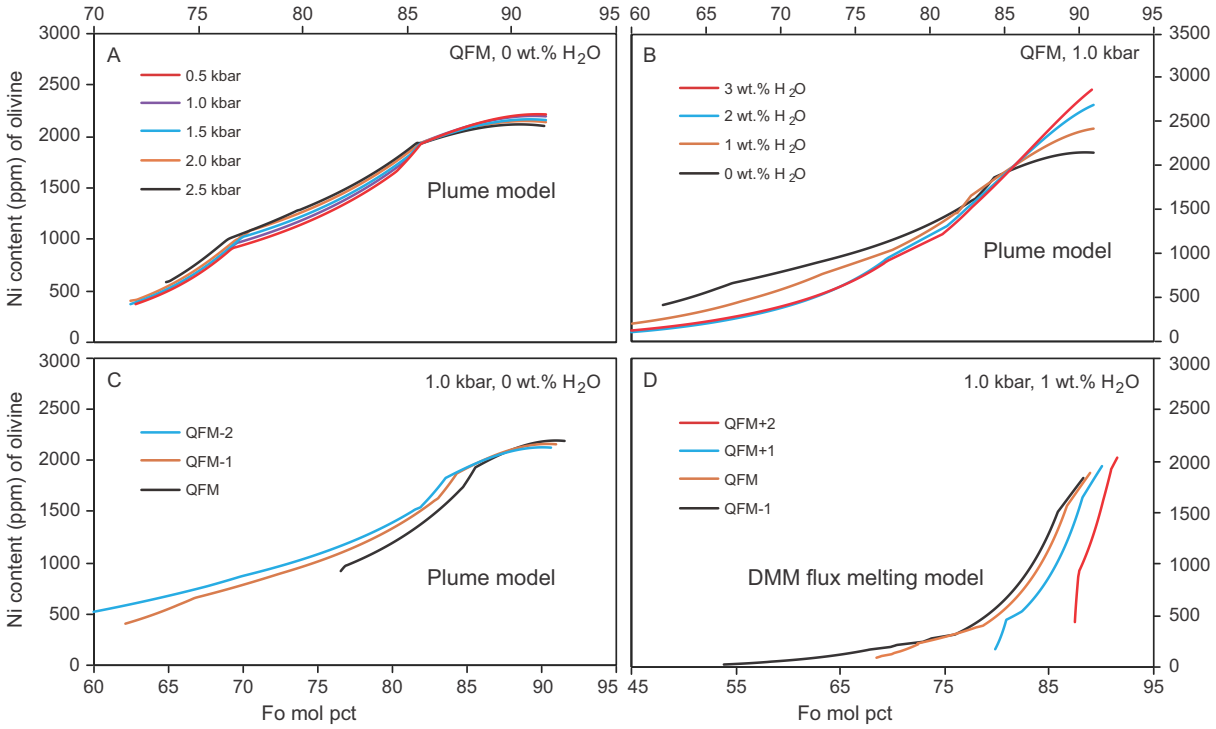
A
QFM, 0 wt.% H2O
0.5 kbar
1.0 kbar
1.5 kbar
2.0 kbar
2.5 kbar
Plume model
B
QFM, 1.0 kbar
3 wt.% H2O
2 wt.% H2O
1 wt.% H2O
0 wt.% H2O
Plume model
C
1.0 kbar, 0 wt.% H2O
QFM-2
QFM-1
QFM
Plume model
D
1.0 kbar, 1 wt.% H2O
QFM+2
QFM+1
QFM
QFM-1
DMM flux melting model
Ni content (ppm) of olivine
Fo mol pct